Spatiotemporal Mapping of Tertiary Lymphoid Structure Heterogeneity Shapes Immune Niches and Clinical Outcomes in Intrahepatic Cholangiocarcinoma

Authors

Liaoliao Gao[1#], Jie Mei[2, 3#], Libing Hong[1#], Yuzhi Jin[1#], Jinlin Cheng[4], Xuqi Sun[1], Chuan Liu[1], Bin Li[1], Xiaomeng Dai[1, 5], Bo Lin[6,7], Yajie Sun[8], Peng Zhao[1, 5], Minshan Chen[2, 3], Rongping Guo[2, 3], Shan Xin[9], Jingping Yun[3, 10], Inmaculada Martínez-Reyes[11, 12, 13], Wei Wei[2, 3*], Weijia Fang[1, 5*], Xuanwen Bao[1, 5*]

Affiliations

[1]Department of Medical Oncology, The First Affiliated Hospital, Zhejiang University School of Medicine, Hangzhou, China.

[2]Department of Liver Surgery, Sun Yat-sen University Cancer Center, Guangzhou, China.

[3]State Key Laboratory of Oncology in South China, Collaborative Innovation Center for Cancer Medicine, Guangdong Provincial Clinical Research Center for Cancer, Sun Yat-sen University Cancer Center, Guangzhou, China.

[4]State Key Laboratory for Diagnosis and Treatment of Infectious Diseases, The First Affiliated Hospital, Zhejiang University School of Medicine, Hangzhou, China.

[5]National Key Laboratory of Advanced Drug Delivery and Release Systems, Zhejiang University, Hangzhou, China.

[6]School of Software, Zhejiang University, Ningbo, China.

[7]Innovation Centre for Information, Binjiang Institute of Zhejiang University, Hangzhou, China.

[8]Cancer Center, Union Hospital, Tongji Medical College, Huazhong University of Science and Technology, Wuhan, China.

[9]Department of Genetics, Yale School of Medicine, New Haven, USA.

[10]Department of Pathology, Sun Yat-sen University Cancer Center, Guangzhou, China.

[11]German Cancer Research Center (DKFZ), Heidelberg, Germany.

[12]German Cancer Consortium (DKTK), partner site Berlin, a partnership between DKFZ and Charité-Universitätsmedizin Berlin, 10117 Berlin, Germany.

[13]Department of Hematology, Oncology and Cancer Immunology, Campus Benjamin Franklin, Charité - Universitätsmedizin Berlin, corporate member of Freie Universität Berlin and Humboldt-Universität zu Berlin, 12203 Berlin, Germany.

[#]These authors contributed equally to this work.

[*]Corresponding Authors: xuanwen.bao@zju.edu.cn (Xuanwen Bao), weijiafang@zju.edu.cn (Weijia Fang), weiwei@sysucc.org.cn (Wei Wei)

Abstract

Intrahepatic cholangiocarcinoma (iCCA) is a highly lethal malignancy with limited therapeutic options. The spatial architecture and functional diversity of tertiary lymphoid structures (TLSs) in iCCA remain unclear. Here, we present a multimodal spatial atlas of TLSs and identified Intra-tumoral TLSs (iTLSs) as independent prognostic markers. Bulk proteomic profiling of 214 discovery and 155 validation cases identified a four-tier TLS-based TME classification system and supported development of a TLS-predictive random forest classifier. Imaging mass cytometry revealed that iTLS$^+$ tumors harbor structured immune architectures, where M1-like tissue-resident macrophages (RTMs), dendritic cells, and CXCL13$^+$ CD4$^+$ T cells co-localize to form antigen-presenting neighborhoods (apc-CNs) spatially coupled to TLS core regions (TLScore-CNs). Single-cell spatial transcriptomics further resolved 61 TLSs into 14 spatial niches and defined a pseudo-temporal maturation continuum: aggregated, activated, and post-activated. Intra-niche communication, primarily mediated by ifnCAFs, iCAFs, and CXCL12$^+$ macrophages, evolved dynamically with maturation. Single-nucleus RNA-sequencing combined with Tangram-based spatial mapping revealed CXCL12$^+$ macrophages and iCAFs forming a peripheral band in aggregated TLSs, while ifnCAFs infiltrated TLS interiors during activation. These findings define TLS heterogeneity and provide insights for stroma-directed immunotherapy.

Teaser

An atlas of tertiary lymphoid structures reveals immune-stroma interactions in Intrahepatic cholangiocarcinoma.

MAIN TEXT

Introduction

Intrahepatic cholangiocarcinoma (iCCA), the second most common primary liver malignancy, is marked by aggressive clinical behavior and pronounced molecular heterogeneity, posing significant challenges for effective therapeutic management (*1*). Despite the advent of PD-(L)1 blockade and targeted agents, clinical benefits remain limited to specific subsets of patients (*2*), underscoring the need for a deeper understanding of tumor microenvironmental (TME) features that could inform more precise therapeutic stratification.

Tertiary lymphoid structures (TLSs) have emerged as key immunological components within the TME, with accumulating evidence across multiple cancer types supporting their role in antitumor immunity and their predictive value for immunotherapy response (*3*). In iCCA and related hepatobiliary malignancies, TLSs exhibit striking heterogeneity in both spatial distribution and maturation status, with functional consequences for local immune responses (*4-8*).

Specifically, intratumoral TLSs—particularly follicular structures containing germinal centers—have been associated with improved patient survival and enhanced recruitment of CXCL13^{+} CD4^{+} T cells, reflecting a capacity to support productive T–B cell interactions (*9*). In contrast, peritumoral TLSs may contribute to immunosuppression via Treg enrichment, and immature aggregates (Agg) often lack prognostic significance, highlighting the functional divergence of TLS subtypes.

This prognostic paradigm of TLS heterogeneity is recapitulated in other malignancies. In hepatocellular carcinoma, immature TLSs can be further stratified into conforming and deviating forms, with only the former exhibiting responsiveness to immunotherapy on par with mature TLSs (*10*). Similarly, in high-grade serous ovarian cancer, the spatial maturity of TLSs varies markedly across anatomical sites, with more developed structures correlating with increased immune activity and improved outcomes (*11*). These findings converge on the notion that the spatial architecture, developmental trajectory, and immune functionality of TLSs collectively determine their clinical relevance and therapeutic implications.

Despite these insights, a systematic, high-resolution atlas of TLS heterogeneity in iCCA has yet to be established. To address this, we employed an integrative spatial multi-modal approach, combining bulk and spatial proteomics, single-nucleus RNA sequencing (snRNA-seq), and imaging mass cytometry (IMC) with single-cell spatial transcriptomics. Through this spatial multi-modal framework, we identified four TLS-based TME subtypes—Desertic, Excluded, Immature, and Structured—defined by distinct TLS morphologies and spatial features. Among them, the Structured subtype, characterized by intratumoral TLSs (iTLS), emerged as an independent prognostic marker.

Subtype-specific proteomic signatures enabled construction of a predictive random forest classifier, while paired IMC provided high-resolution maps of spatial architectures. Single-cell spatial transcriptomics further delineated the molecular identity of TLSs, uncovering subtype-specific cellular compositions and pseudo-time dynamic remodeling of spatial niche networks within the TME. snRNA-seq provided active signaling pathways and enabled high-resolution spatial mapping, revealing subtype-specific transcriptional programs. Together, these findings establish a multidimensional framework for understanding spatiotemporal TLS diversity in iCCA, offering insights into its prognostic relevance and potential therapeutic leverage points.

Results

Comprehensive Landscape of TLS Distribution and Classification in iCCA

We conducted a spatial and morphological assessment of TLSs in tumor samples from 214 patients with iCCA (Figure 1A, Table S1). Histological evaluation and staining with CD20, CD3, CD21, BCL6, and Ki67 were used to classify TLSs into three distinct morphologies: aggregates (Agg), primary follicles (FL1), and secondary follicles (FL2) (Figure 1B–C, Figure S1A-B). Spatial profiling showed that 22.2% of

TLSs were located intratumorally, with the remainder residing in the peri-tumoral stroma. Density distribution analysis revealed a strong positional preference within 5 mm of the tumor boundary (Figure 1D). Morphological mapping using Sankey diagrams revealed distinct configurations of TLS maturation between intra-tumoral and peri-tumoral compartments (Figure 1E). For each patient, TLS morphology was evaluated at both sites, and the most advanced TLS stage observed within each compartment (FL2 > FL1 > Agg > none) was used to represent that patient's status. iTLS were detected in 28% patients with mature TLS (FL1 and FL2) existing in most cases, while pTLS were observed in 77% patients with immature (Agg) and mature TLS evenly evaluated.

Based on these patterns, we devised a four-tier TLS-based TME classification system comprising: the Structured subtype ($iTLS^+$), Excluded ($iTLS^-/pFL^+$), Immature ($iTLS^-/pAgg^+$), and Desertic ($iTLS^-/pTLS^-$) phenotypes (Figure 1F). This classification showed significant prognostic value, with differences in overall survival (OS, p = 0.00052) and progression-free survival (PFS, $p < 0.0001$) across subtypes (Figure 1G). Notably, patients with Structured TLSs exhibited significantly improved outcomes (OS p = 0.0037; PFS p = 0.00018). In multivariate analysis adjusted for clinical covariates, the presence of iTLS was independently associated with better OS (HR = 0.52, 95% CI: 0.33–0.82, p = 0.005) and PFS (HR = 0.52, 95% CI: 0.35–0.77, p = 0.001) (Figure 1H).

Proteomic Profiling Reveals TLS-Associated Immune Subtypes

To investigate the molecular correlates of TLS heterogeneity, we performed multi-omics profiling across a discovery cohort (n = 214) and additional validation cohorts, including spatial proteomics and paired imaging mass cytometry (IMC) (n = 155, Table S2), single-nucleus RNA sequencing (snRNA-seq, n = 14), and spatial transcriptomics (10x Xenium in situ, n = 5). Mass spectrometry–based bulk proteomics enabled construction of a TLS-predictive random forest classifier, which was subsequently validated using expansion-gel spatial proteomics (n = 155) (Figure 2A). To allow spatially matched validation, expansion-gel spatial proteomics and IMC were performed on serial tissue sections from the same specimens. Regions of interest (ROIs) were precisely co-registered across modalities to ensure that spatial proteomic data and IMC data were derived from the same anatomical context. IMC was used to delineate the single-cell spatial architectures of TME subtypes, while 10x Xenium whole-slide spatial transcriptomics enabled comprehensive TLS profiling at tissue scale with subcellular resolution. In parallel, snRNA-seq profiles were applied to spatially mapped onto Xenium spatial transcriptomic coordinates for high-resolution projection and uncover subtype-specific transcriptional programs.

Distinct proteomic signatures were identified across TLS-based TME subtypes (Figure 2B). Structured TLSs were enriched for lymphoid-associated molecules, including CR2, CD19, and MS4A1, along with chemokines such as CXCL13. In contrast, Desertic tumors exhibited increased expression of epithelial and metabolic

markers, notably KRT4. Pathway enrichment analysis highlighted subtype-specific immune activity: Structured TLSs showed enhanced immune activation, including CD28 co-stimulation, S1PR4 signaling, and IL-12 response pathways, whereas Desertic tumors exhibited dominant signatures of hypoxia, epithelial–mesenchymal transition (EMT), and coagulation (Figure 2C).

To further validate these subtype-specific immune landscapes, we applied a previously published TLS-related gene signature (*12*) (Table S3) to derive a proteomics-based TLS score. Structured tumors exhibited the highest TLS scores, while Desertic tumors had the lowest (Figure S2A), supporting the subtype classification. GO analysis of differentially expressed proteins among the four subtypes revealed that Structured tumors were enriched for immune-activated pathways—such as B cell receptor signaling, leukocyte proliferation, T cell selection, and immune homeostasis—while Desertic tumors showed upregulation of coagulation, reactive oxygen species metabolism, complement activation, and extracellular matrix remodeling (e.g., cell–substrate adhesion) (Figure S2B). Volcano plot and enrichment analysis highlighted functional immune divergence: iTLS$^+$ tumors displayed activation of antigen receptor–mediated signaling, T cell receptor signaling, regulation of B cell proliferation and chemokine signaling (Figure S2C–D). In contrast, iTLS$^-$ tumors showed upregulation of ECM reorganization, metabolic reprogramming, and cell cycle–related pathways, including p53 signaling (Figure S2E).

Given the pronounced survival advantage observed in iTLS$^+$ tumors, we next asked whether proteomic profiles could effectively distinguish iTLS$^+$ from iTLS$^-$ samples. We therefore constructed a random forest classifier to predict iTLS status based on protein expression features derived from the discovery cohort. The dataset was randomly split 3:1 into training and testing sets and evaluated using five-fold cross-validation. The model achieved a training AUC of 84.5% and a testing AUC of 90.1% ($p < 0.001$) (Figure 2D), with permutation control confirming specificity (Figure 2E). Top discriminative proteins included MS4A1, CR2, TCL1A, BANK1, ADRA2A, and CXCL13 (Figure 2F), many of which were also prognostically significant in univariate survival analyses (Figure 2G). External validation in an independent cohort using expansion-gel spatial proteomics combined with IMC achieved an AUC of 92.5%, further supporting model generalizability (Figure 2H–I).

In validation cohort, IMC-based mapping first revealed distinct major cell populations and their finer subdivision into subsets based on specific markers, as shown in Supplementary Figure S3A-C. These analyses identified immune cell subsets and their spatial distribution across the tumor microenvironment. The characterization of these populations allowed us to further investigate the immune landscape in iCCA and correlate it with the TME subtypes. Structured subtypes showed organized lymphoid aggregation, while Excluded and Immature subtypes displayed compartmentalized immune architecture. Desertic tumors exhibited sparse immune infiltration dominated by stromal and epithelial cells (Figure 2J). Notably, the structured subtype revealed a

206 significant clustering of T and B cells within the TLS region ROI, highlighting the
207 organized immune architecture characteristic of mature TLS (Figure 2J and Figure
208 S3D).
209
210 **Single-cell Spatial Architecture of TLS-Enriched Tumor Microenvironments**
211 To investigate how immune spatial architecture differs across TLS-defined TME
212 subtypes, we performed IMC to resolve single-cell spatial features within
213 representative tumor regions. IMC was applied to rigorously selected ROIs
214 representing TLSs, immune-infiltrated areas, and stromal compartments (Figure 3A).
215 Survival analysis at whole-slide level in the validation cohort recapitulated subtype
216 associations with OS (p = 1e^{-04}) and confirmed prognostic value of iTLS presence (p
217 = 0.00011) (Figure 3B).
218 Structured TME featured densely intermingled T and B cells forming tightly
219 compacted aggregates resistant to sub-clustering, a hallmark of mature TLS
220 organization. Surrounding immune-rich zones were enriched for specialized T cell
221 subsets, including CXCL13$^+$ memory CD4$^+$ T cells, CD127$^+$ and PD1$^+$ CD4$^+$ T cells,
222 and naïve CD4$^+$ T cells (Figure 3C). Expression gradients of CD20, CD45RO, and
223 CD45RA further validated the spatial stratification (Figure 3D), corroborated by
224 spatial proteomics mapping of CXCL13 and CCL19 (Figure 3E).
225 Spatial proximity analyses highlighted M1-like RTMs as key architectural hubs,
226 forming tight associations with both T/B clusters and CXCL13$^+$ CD4$^+$ T cells (Figure
227 3F). Structured tumors exhibited the closest interactions, while Desertic subtypes
228 were characterized by dispersed and poorly connected immune compartments (Figure
229 3G). DCs also localized near TLSs, though at slightly increased distances compared to
230 M1-like RTMs (Figure 3F–G). Lastly, M1-like RTMs and DCs showed greatest cell
231 proximity to T cell subpopulations than other myeloid cells (Figure 3H). These
232 findings position M1-like RTMs and DCs as organizational anchors in TLS spatial
233 hierarchies.
234
235 **TME Subtype-Specific Spatial Context Networks**
236 To further dissect intercellular interactions, we conducted spatial analyses integrating
237 Effective Score (ES), pairwise cell interaction (PCI), and cellular neighborhood (CN)
238 mapping (Figure 4A). M1-like RTMs and DCs showed peak ES in TLS regions of
239 Structured tumors, suggesting their functional compartmentalization within mature
240 TLSs (Figure 4B). PCI mapping confirmed their privileged proximity to CXCL13$^+$
241 CD4$^+$ T cells and T/B clusters (Figure 4C).
242 CN analysis revealed two functionally distinct but spatially coupled neighborhoods:
243 CN8, comprising T cells with M1-like RTMs and DCs (apc-CN), and CN19,
244 representing organized T/B cell aggregates (TLScore-CN) (Figure 4D). Regional
245 enrichment analyses demonstrated that CN19 localized specifically to TLS regions,
246 whereas CN8 was predominant in peri-TLS immune cell-enriched zones (Figure 4E).
247 Multicellular neighborhood interfaces may reflect coordinated immune functions

within the TME. To quantify and formalize spatial associations between CNs, we applied a spatial context framework adapted from prior studies(*13, 14*). iTLS^{-} tumors exhibited higher degrees of compartmentalization compared to iTLS^{+} tumors (Figure 4F, top row), suggesting a more homogeneous and spatially segregated immune composition. In contrast, CNs such as apc-CN and TLScore-CN showed greater spatial dominance and compartmental stability in iTLS^{+} tumors, indicative of coordinated expansion of APC–T cell–rich TLS regions (Figure 4F, top row). These CNs transformed large tumor regions into structured immune hubs with conserved cell-type compositions.

Spatial windows composed of ≥85% from two CNs were used to define functionally meaningful CN interfaces. iTLS^{+} tumors showed higher frequencies of apc-CN and TLScore-CN co-occurrence compared to iTLS^{-} tumors, where CN pairing appeared more stochastic (Figure 4F, middle row). This suggests that the local compositional balance between these immune neighborhoods may be more functionally relevant than global cell abundance averages.

To further quantify this, we analyzed the relative proportions of apc-CN, TLScore-CN, and other major immune CNs within spatial windows enriched for these interactions (≥85%) (Figure 4G). A dominant interface of apc-CN and TLScore-CN emerged in iTLS^{+} tumors (Figure 4G), which was visibly localized when CNs were spatially mapped (Figure 4G, pink and chestnut red), highlighting their consistent juxtaposition within Structured TLS regions. Furthermore, CN9 (Endothelium enriched) displayed prominent spatial interactions with CN19 (TLScore-CN) and CN8 (T&APC enriched) in iTLS^{+} tumors. This finding is consistent with the observed colocalization of TLSs and vascular structures, suggesting that endothelial neighborhoods may support the formation and organization of TLS-associated immune microenvironments through vascular-immune crosstalk.

These data support a sequential model of TLS organization, wherein antigen presentation and CD4^{+} T cell activation by M1-like RTMs and DCs in CN8 precede the recruitment and spatial organization of lymphocytes into CN19, ultimately establishing mature TLS architecture.

Single-cell Spatial Transcriptomics Uncovers Molecular States of TLS

Our initial multimodal profiling—combining histopathology, bulk proteomics, and IMC—revealed broad immune heterogeneity in iCCA, with spatial distribution of TLSs correlating with distinct TME landscapes. While IMC identified major TLS-associated neighborhoods, such as dense T/B cell clusters, its limitations in marker depth and spatial throughput precluded fine-resolution dissection of TLS molecular programs. To overcome these constraints, we employed high-content spatial transcriptomics using 10x Genomics Xenium, enabling transcriptome-wide subcellular profiling across intact tissue.

We profiled 433,051 cells from five iCCA samples (4 iTLS^{+}, 1 iTLS^{-}), with detailed annotation of immune, stromal, and epithelial compartments (Figure 5A–D). TLS-rich

zones showed spatially restricted expression of canonical markers (e.g., CXCL13, MS4A1, CR2, CD3E), aligned with cell mask boundaries (Figure 5B). Major cell types and their subtypes—including distinct T cell, B cell, stromal, and myeloid lineages—were resolved at high resolution (Figure 5C–D). Dot plots of marker gene expression validated both major lineages and finer subdivisions (Figure S4A–B).

We next identified 61 TLS structures across samples using combined spatial and transcriptomic criteria. Based on histological evaluation, 33% were classified as Agg, 46% as FL1, and 21% as FL2 (Figure S5A). Treating each TLS as a pseudo-bulk unit, we performed PCA on their aggregated gene expression profiles. Principal components PC1 and PC2 captured substantial molecular heterogeneity (Figure 5E), and expression gradients of key TLS-related genes (e.g., CXCL12, CXCL13, BANK1, CR2, RORC, IRF8) revealed continuous, rather than discrete, diversity (Figure 5F; extended in Figure S4C).

Based on PCA positioning and molecular signatures, we stratified TLSs into three pseudo-temporal transcriptional states: Aggregated, Activated, and Post-activated (Figure 5G). Transcriptomic profiling revealed that 44% of TLSs were Aggregated, 25% were Activated, and 31% were Post-activated (Figure S5A). While these subtypes partially overlapped with conventional histology (Agg, FL1, FL2), significant intra-class variability highlighted the added granularity of transcriptomic classification (Figure 5H). Abundance analysis of constituent cell types further distinguished these molecular states: Aggregated TLSs were enriched in $CXCL12^+$ macrophages, plasma cells, and iCAFs; Activated TLSs featured $CXCL13^+$ $CD4^+$ T cells; and Post-activated TLSs were characterized by $TCF7^+$ $CD4^+$ T cells and Tregs (Figure 5I). To explore the spatial distribution of TLS maturation states relative to tumor architecture, we measured the distances from each TLS (Aggregated, Activated, and Post-activated) to the nearest tumor boundary (Figure S5B). The analysis revealed that Aggregated and Activated TLSs tended to localize closer to the tumor margin, whereas Post-activated TLSs were more frequently positioned at greater distances from the tumor margin. This spatial pattern suggests that TLS maturation may initiate near the invasive front, where immune–tumor interactions are most active, and subsequently progress toward more organized, distal immune regions. These findings suggest a coordinated progression from stromal priming to immune activation and eventual regulatory consolidation.

Spatiotemporal Niche Rewiring and Intercellular Signaling Define TLS Maturation

To elucidate how TLSs mature within the iCCA tumor microenvironment, we systematically mapped 14 spatially resolved cellular niches across the pseudo-temporal trajectory of TLS progression—Aggregated, Activated, and Post-activated. Each TLS stage exhibited distinct niche compositions and organizational architectures (Figure 6A–B). Aggregated TLSs were enriched for niches containing iCAFs and $CCL19^+$ $CD8^+$ T cells, as well as antigen-presenting niches harboring cDC2 and

CXCL12$^+$ macrophages. In contrast, Activated TLSs displayed marked expansion of niches enriched in memory B cells, CXCL13$^+$ CD4$^+$ T cells, IFN-producing CAFs, mregDCs, and GZMK$^+$ CD8$^+$ T cells, consistent with a transition toward coordinated immune activation. Post-activated TLSs were dominated by regulatory niches composed of TCF7$^+$ CD4$^+$ T cells, Tregs, and germinal center–like regions populated by naïve and proliferating B cells (Figure S5C-D).

To further dissect the spatial coordination of immune compartments, we performed niche-level interaction network analysis, revealing that germinal center and memory B cell zones formed distinct niche–niche interaction hubs at each TLS stage (Figure 6C). In the aggregated subtype, niche connectivity analysis identified significant spatial interactions between iCAF & CCL19$^+$ CD8$^+$ T cell-enriched niches and both memory B cells & CXCL13$^+$ CD4$^+$ T cell-enriched niches and cDC2 & CXCL12$^+$ macrophage-enriched niches. While the activated subtype exhibited reorganization of the interaction landscape, where memory B cells & CXCL13$^+$ CD4$^+$ T cell-enriched niches occupied central network positions and demonstrated enhanced connectivity with diverse partners including IFN-producing CAFs, mregDCs, and GZMK$^+$ CD8$^+$ T cell-enriched niches and other niches, collectively highlighting subtype-specific topological shifts during TLS functional progression. Supplementary Figure S5E further validates this shift by mapping cell–cell network interactions across TME subtypes, complementing niche-level architecture described in Figure 6C.

Hallmark pathway enrichment further demonstrated functional divergence across TLS states (Figure 6D). Aggregated TLSs were enriched for angiogenesis and TGF-β signaling pathways, while Activated TLSs showed prominent interferon responses (IFN-α, IFN-γ), IL-10 signaling, PD-1 pathway activation, and CD3/TCR phosphorylation. Post-activated TLSs exhibited heightened signatures of oxidative stress (ROS pathway), TNF-α signaling via NF-κB, inflammatory responses, and IL6–JAK–STAT3 activation, suggesting immunoregulatory consolidation. Differential expression analysis supported these patterns, with Aggregated TLSs expressing higher levels of CXCL6, Activated TLSs upregulating CR2, CXCL9, and LAMP3, and Post-activated TLSs marked by increased IL6 and CCN1 (Figure 6E).

To investigate intra-niche signaling, we mapped cellular communication networks across TLS maturation states (Figure 6F). We identified strong intra-niche communication circuits where major sender cell types—such as IfnCAF, iCAF, CXCL12$^+$ macrophages, and CCL19$^+$ CD8$^+$ T cells—engaged with recipient cells localized within the same niche microenvironment (Figure 6F, top panel). Furthermore, dynamic shifts were found in dominant signaling cell populations: Aggregated TLSs were characterized by prominent signaling from CXCL12$^+$ macrophages and iCAFs, while Activated TLSs showed a transition to IFN-producing CAFs as the primary signal senders (Figure 6F, top panel). Notably, CXCL12-mediated signaling exhibited stage-specific patterns - in Aggregated TLSs, CXCL12 signals originated predominantly from macrophages and iCAFs; during the Activated phase, IFN-producing CAFs became the main CXCL12 source; and in Post-activated

TLSs, CXCL12 signaling became more evenly distributed across multiple cell types (Figure 6F, bottom panel). These tightly compartmentalized signaling patterns delineate a spatially organized mechanism whereby niche-specific immune communication orchestrates both microenvironment construction and phase transition during TLS development.

Collectively, these findings define a spatiotemporal trajectory of TLS maturation, transitioning from stromal priming to immune activation and ultimately regulatory consolidation, orchestrated through dynamic niche rewiring and stage-specific intercellular communication networks.

snRNA-seq and Spatial Mapping Reveal TLS-Associated Immune Topologies

To further validate the spatial and functional signatures identified via IMC and Xenium, we performed single-nucleus RNA sequencing using the 10x Genomics Chromium Flex platform, which offers significantly higher gene detection sensitivity per cell compared to Xenium, across 14 iCCA samples (8 iTLS$^+$, 6 iTLS$^-$) (Figure 7B). Desertic-type iTLS$^-$ tumors were selected for snRNA-seq to establish a TLS-free baseline. Importantly, we included cases with detectable immune infiltration to ensure sufficient representation of immune subsets for meaningful transcriptional comparison with iTLS$^+$ samples. A total of 105,226 cells were profiled, encompassing major compartments including T cells, B cells, myeloid cells, stromal cells, endothelial cells, epithelial cells, cycling cells, and hepatocytes. Refined clustering identified six T cell subsets (e.g., TCF7$^+$ CD8$^+$ T cells, CXCL13$^+$ CD4$^+$ T cells), three B cell subsets (naive B, memory B, and germinal center B cells), four stromal subsets (iCAF, ifnCAF, myoCAF, and pericyte), and twelve transcriptionally distinct myeloid populations (e.g., cDC1, cDC2, CD16$^+$ monocytes, CXCL12$^+$ macrophages) (Figure 7C). Cross-platform validation via dot plots in Supplemental Figure S6A–E confirmed concordance between Xenium and 10x Flex in identifying these subsets, with the latter exhibiting superior gene detection sensitivity (Figure S6A-E).

Ro/e analysis revealed preferential accumulation of T cells, B cells, and plasma cells in iTLS$^+$ tumors, whereas stromal, endothelial, epithelial, and myeloid cells were more abundant in iTLS$^-$ tumors (Figure 7D). At the subset level, immune populations associated with memory and helper functions, including TCF7$^+$ CD8$^+$ T cells, memory B cells, and CXCL13$^+$ CD4$^+$ T cells with TFH-like properties, were enriched in iTLS$^+$ tumors. Antigen-presenting cells such as cDC1, cDC2, and CXCL12$^+$ macrophages were also more prevalent in the iTLS$^+$ group. In line with spatial transcriptomics results, stromal subsets including iCAF and ifnCAF showed increased abundance in iTLS$^+$ tumors (Figure 7D).

We further dissected the functional polarization of CXCL12$^+$ macrophages, which exhibited elevated activities of antigen presentation pathway and M1-related pathway (Figure S6F). Comparative analysis of M1/M2 gene sets confirmed their M1-like phenotype, distinct from other monocyte-derived macrophages (Figure S6G). Notably,

415 these cells scored highest for an M1-RTM signature derived from prior work (Figure
416 S6H), underscoring their role in early TLS initiation.
417 We next applied Tangram to spatially map the single-nucleus RNA-seq profiles onto
418 Xenium spatial transcriptomic coordinates, thus enabling high-resolution projection of
419 transcriptionally defined cell types and at the same time expanding the gene
420 throughput in spatial tissue architecture (Figure 7E). This integration compensated for
421 Xenium's limited gene detection by precisely localizing 10x Flex-defined states and
422 their associated pathways. To evaluate the accuracy of spatial mapping between
423 single-nucleus RNA-seq and Xenium spatial transcriptomics, we performed quality
424 control based on Tangram projection metrics. The distribution of training scores
425 indicated overall robust alignment between modalities, with most cells exhibiting high
426 mapping confidence (Figure S7A, left). Sparsity analyses further validated mapping
427 consistency, showing expected relationships between cellular sparsity and spatial
428 signal distribution (Figure S7A, middle and right). Spatial prediction scores were
429 inversely correlated with pixel-level sparsity, yielding a global AUC of 0.704 (Figure
430 S7B), supporting the reliability of Tangram integration. Finally, mapped cell-type
431 compositions across TME subtypes recapitulated biologically coherent patterns
432 demonstrating the spatial fidelity of projection (Figure S7C).
433 We revealed that iCAF, and CXCL12^{+} macrophages were predominantly enriched in
434 Aggregated TLSs and localized to the peripheral regions of TLS structures, whereas
435 CXCL13^{+} CD4^{+} T cells, memory B cells, and ifnCAFs were more abundant in
436 Activated TLSs. Notably, iCAF and ifnCAF populations formed a ring-like peripheral
437 organization in Aggregated TLSs, which progressively infiltrated into the TLS core in
438 Activated TLSs, reflecting a potential stromal remodeling process.
439 To further validate the spatial allocation of key cell types across TLS maturation
440 states, we assigned each Xenium-detected cell to its most probable snRNA-seq–
441 defined identity and performed a OR analysis across the 61 TLSs (Figure 7F). The
442 distributions confirmed the expected localization patterns observed in earlier
443 analyses—for example, iCAF, CXCL12^{+} macrophages predominated in Aggregated
444 TLSs, while mregDCs were enriched in Activated TLSs—thereby supporting the
445 spatial validity of the Xenium-based classification framework. The signature scores
446 across mapped cells were further calculated. The M1-RTM signature, derived from
447 macrophages with M1-like tissue-residency properties (*5*), was predominantly
448 enriched in Aggregated TLSs, indicating the early involvement of CXCL12^{+}
449 macrophages in TLS initiation (Figure 7F). In contrast, the APC signature peaked in
450 Activated TLSs, suggesting that robust antigen presentation programs emerge later as
451 TLSs transition into functionally active immune niches.
452 Together, these integrated results from Xenium and 10x Flex reveal the dynamic
453 spatial reorganization of stromal and immune compartments across TLS
454 developmental states. In combination with IMC-derived spatial CNs, these findings
455 reinforce the model in which antigen presentation and CD4^{+} T cell activation by M1-
456 like RTMs and DCs in early-stage TLS regions precede lymphocyte aggregation and

organization into TLScore-CNs, ultimately establishing mature TLS structures. Spatial localization of DCs and CXCL12$^+$ macrophages at TLS peripheries in Aggregated states further implicates them as early orchestrators of TLS nucleation.

Key TLS-Associated Niches Predict Immunotherapy Response

To explore the potential relevance of TLS-associated spatial niches in predicting immunotherapy efficacy, we investigated the prognostic value of five key niches—N3 (cDC2 & CXCL12$^+$ Mac enriched), N4 (GC B & Naïve B enriched), N5 (iCAF & CCL9$^+$ T & Mac enriched), N10 (ifnCAF, mregDC & GZMK$^+$ CD8$^+$ T enriched), and N13 (Memory B & CXCL13$^+$ CD4$^+$ T enriched)—previously implicated in TLS molecular remodeling across the Aggregated to Post-activated continuum. Using three publicly available bulk RNA-seq datasets from immune checkpoint blockade–treated cohorts (GSE91061, GSE126044, and PRJEB23709), which include clinical outcome data from melanoma and non–small cell lung cancer patients, we computed niche-specific signature scores to each cohort. Across all datasets, we observed consistent enrichment of these niche signatures in responders compared to non-responders, indicating their association with favorable therapeutic responses (Figure 8A). Moreover, elevated expression of niche-specific signatures correlated with prolonged overall survival, suggesting that transcriptional features reflective of these spatial niches may serve as conserved biomarkers of effective anti–PD-1–mediated immune engagement (Figure 8B-D). These results suggest that TLS-centric spatial programs may contribute to effective antitumor immunity and serve as predictive markers of immunotherapy benefit. Additionally, we analyzed the additional TLS-associated niches, N8 (plasma cell, CXCL9$^+$ T and macrophage-enriched), N12 (T/Mac-enriched), and N14 (TCF7$^+$ CD4$^+$ Treg-enriched), across all three immunotherapy-treated RNA-seq cohorts (Figure S8). Among these, N8 exhibited significant enrichment in responders and improved survival only in the PRJEB23709 cohort, while the other two datasets showed nonsignificant trends, suggesting potential cohort-dependent activation of this effector-like niche. In contrast, both N12 and N14 displayed consistent and robust patterns across all three datasets: their signature scores were significantly higher in responders and correlated with better overall survival, indicating that these niches may reflect coordinated immune activation rather than immune suppression. These results reinforce that distinct TLS-associated niches display heterogeneous relationships with immunotherapy response and survival outcomes.

Finally, we summarized the contrasting tumor microenvironmental features of iTLS-positive and iTLS-negative patients and furtherly proposing a spatiotemporal model of TLS maturation (Figure 9). This maturation continuum highlights how coordinated T/B-cell aggregation and chemokine-driven activation sculpt functional immune niches within iTLS-positive tumors. Together, this model provides a conceptual framework linking TLS evolution to the development of functional immune niches and potential therapeutic responsiveness in iCCA.

Discussion

Our study presents the first comprehensive spatial atlas of TLSs in iCCA, unveiling their remarkable molecular and architectural heterogeneity. By classifying iCCA into four distinct immune subtypes based on TLS spatial and morphological features, we propose a novel framework for interpreting tumor–immune interactions. Notably, the identification of the Structured subtype, characterized by the presence of iTLS, as an independent prognostic factor highlights that it is the spatial configuration—rather than the mere presence—of TLSs that dictates clinical outcome. This observation is consistent with findings in other tumor types (*6*), while also revealing iCCA-specific patterns in TLS biology.

To achieve a multidimensional understanding of TLS heterogeneity, we implemented an integrative, multimodal strategy combining bulk and spatial omics platforms. Bulk proteomics enabled large-scale molecular stratification and served as the basis for TME subtype classification via a random forest model. IMC offered single-cell spatial resolution but was limited in multiplexing and tissue throughput. Expansion-based spatial proteomics provided broader cohort-level coverage, albeit at pseudo-bulk resolution. To resolve intra-TLS cellular architecture, we applied single-cell spatial transcriptomics, allowing high-resolution classification of immune and stromal subsets. Given its lower gene detection sensitivity, we further incorporated single-nucleus RNA sequencing to enhance transcriptomic depth and resolve functional programs. Through coordinated use of these complementary technologies, we captured TLS-associated features at multiple molecular and spatial scales—enabling cross-validation of cell types, spatial niches, activation states, and communication networks. This multimodal integration not only reinforces the robustness of our findings but also establishes a scalable framework for decoding complex immune ecosystems in solid tumors.

Our spatial proteomic and transcriptomic analyses underscore the requirement for precise cellular architecture in the formation of functional TLS niches. Specifically, M1-like RTMs, DCs, and T cells form highly organized apc-CN, which spatially interact with TLScore-CN. This architectural coordination recapitulates the microanatomy of lymph nodes, suggesting a conserved paradigm of immune cell orchestration across secondary and ectopic lymphoid sites. The identification of apc-CN as key regulatory hubs within TLS ecosystems offers several mechanistic insights. First, transcriptional analysis via snRNA-seq revealed enrichment of antigen presentation pathways in $CXCL12^+$ macrophages (M1-like RTM phenotype) and DCs, implicating their role in local T cell priming. Second, their close spatial proximity to $CXCL13^+$ $CD4^+$ T cells suggests a function in maintaining TLS-associated chemokine gradients (e.g., CXCL12, CXCL13) (*15, 16*). Third, their interaction networks with TLScore-CN imply potential support for humoral immunity (*17, 18*). These findings

complement recent work showing myeloid-dependent TLS activities (*3*), while revealing iCCA-specific organizational patterns.

Leveraging Xenium spatial transcriptomics, we further resolved TLSs into a pseudo-temporal continuum of molecular subtypes—aggregated, activated, and post-activated. Early stages were dominated by niches co-enriched for iCAFs, CCL19^{+} CD8^{+} T cells, and APC-like myeloid subsets, including cDC2s and CXCL12^{+} macrophages, which formed coordinated spatial interaction networks suggestive of TLS initiation and immune recruitment. As TLSs transitioned to the activated state, niches characterized by CXCL13^{+} CD4^{+} T cells and memory B cells emerged as dominant hubs, indicating progression toward germinal center–like immune architecture.

Interestingly, our observation of TLS subtype based on gene expression can only partially align with TLS maturity identified by HE staining morphology. This suggested that traditional clustering strategy for TLS maturity is insufficient to distinguish TLSs which are pre-activated or post-activated. This claimed the necessity to develop more reliable methods for TLS clustering, which was significantly relative to clinical outcome.

To validate and extend these observations, we performed snRNA-seq using the 10x Chromium Flex platform across 14 iCCA samples. This approach enabled fine-grained identification of TLS-associated immune and stromal subsets, including CXCL13^{+} CD4^{+} T cells, memory B cells, and CXCL12^{+} macrophages. Mapping Flex-derived cell types back onto Xenium spatial coordinates using Tangram revealed strong spatial congruence across platforms. Specifically, CXCL12^{+} macrophages and iCAFs were enriched at the periphery of Aggregated TLSs and formed ring-like distributions, while CXCL13^{+} CD4^{+} T cells and memory B cells infiltrated central TLS regions in Activated states. CXCL12^{+} macrophages exhibited high expression of M1-related genes and scored highest for an M1-RTM signature, reinforcing their role as spatially privileged initiators of TLS nucleation. The secretion of CXCL12, TNF, and IL2RA by CXCL12^{+} macrophages may orchestrate immune cell recruitment and spatial organization—CXCL12 guides cDC2 and lymphocyte positioning, TNF potentiates stromal activation and lymphoid chemokine production (e.g., CCL19, we also identified enrichment of CCL19^{+} T cells in Agg subtype), while IL2RA could modulate local T cell survival, collectively reinforcing TLS aggregation. These results support a stepwise model in which chemokine production, antigen presentation and CD4^{+} T cell activation by M1-like RTMs and DCs precede lymphocyte recruitment and follicular organization, ultimately establishing mature TLS architecture—a model consistent with peripheral apc-CN to TLS-score CN transition defined in our IMC analysis.

Several clinical implications emerge from these findings. Our random forest classifier, derived from proteomic features, may serve as a diagnostic tool for TLS-based tumor stratification. More importantly, mechanistic insights into M1-like RTM and apc-CN function suggest opportunities for therapeutic TLS modulation—either by promoting their spatial assembly or by reprogramming immunosuppressive counterparts. In our

582 previous work, we identified M2-like RTMs as mediators of immunotherapy
583 resistance through suppression of $CD8^+$ T cells, where their spatial proximity to $CD8^+$
584 cells was associated with poor clinical outcomes in iCCA (*5*).Building on these
585 findings, reprogramming M2-like into M1-like RTMs emerges as a rational strategy
586 to enhance anti-tumor immunity. Our integrative framework for TLS classification—
587 spanning morphological, spatial proteomic, and transcriptomic dimensions—provides
588 a potential basis for clinical implementation. The histological markers used to define
589 TLS maturation (CD20, CD3, CD21, BCL6, Ki67) are all compatible with routine
590 IHC platforms and could be adapted for biopsy-level assessment. A semi-quantitative
591 TLS maturity score might therefore serve as a feasible biomarker for identifying
592 iCCA patients with 'immune-hot' tumor microenvironments who are more likely to
593 benefit from immunotherapy. Future studies in biopsy-based cohorts will be needed to
594 evaluate the predictive value and reproducibility of such scoring systems in the
595 clinical setting.
596 This study is not without limitations. Our analyses are primarily observational and
597 descriptive. Future investigations utilizing genetic manipulation models are needed to
598 validate causal relationships between M1-like RTMs and TLS formation. Moreover,
599 longitudinal spatial profiling may clarify whether TLS maturation states represent
600 stable subtypes or transient phases within an evolving tumor-immune ecosystem.
601 In conclusion, our spatial ecosystem analysis redefines the landscape of TLS biology
602 in iCCA. We show that coordinated cellular reorganization and niche-level
603 remodeling underlie TLS heterogeneity, with implications for both biomarker
604 development and therapeutic targeting. These insights offer a foundation for future
605 strategies aiming to harness or reengineer TLSs to overcome immune resistance in
606 this challenging malignancy.
607
608 **Methods**
609 **Histopathological Analysis**
610 All patients in the in-house cohorts were evaluated using standardized protocols. The
611 study was conducted in accordance with the principles of the Helsinki Declaration and
612 received ethical approval from the Medical Ethics Committees of the following
613 institutions: Sun Yat-sen University Cancer Center (SYSUCC) (Approval No.
614 B2024-665-01). The IMC data of the validation cohorts was described in our previous
615 study (*5*). Hematoxylin and eosin (H&E) staining was performed on 4-μm formalin-
616 fixed, paraffin-embedded (FFPE) iCCA tissue sections following standard protocols.
617 After deparaffinization in xylene (3 × 5 min) and rehydration through graded ethanol
618 series (100%, 95%, 75%, 50%; 5 min each), sections were washed in phosphate-
619 buffered saline (PBS, pH 7.4; Solarbio, cat# P1020). Nuclear staining was achieved
620 using Mayer's hematoxylin (Solarbio, cat# G1080) for 5-8 min at room temperature,
621 followed by differentiation in 1% acid ethanol and bluing in 1% ammonium
622 hydroxide (Solarbio, cat# G1822). Cytoplasmic counterstaining employed eosin Y
623 (Solarbio, cat# G1100) for 2 min. Processed sections were dehydrated, cleared in

624 xylene, and mounted with resinous medium (Solarbio, cat# G1402). Whole-slide
625 imaging was conducted using a Pannoramic 250 Flash II Scanner (3D HISTECH) at
626 20× magnification. TLSs were identified on H&E-stained sections as discrete
627 lymphoid aggregates within or adjacent to tumor regions. A structure was considered
628 TLS-positive when contiguous $CD20^+$ and $CD3^+$ lymphocytic clusters exceeded 7,000
629 um^2 in area and contained at least 100 lymphocytes (*19*). TLS maturation was
630 classified into three categories—Agg, FL1, and FL2—based on combined
631 morphological and immunohistochemical criteria. Agg were defined as B and T
632 lymphocytic clusters without clear organization. FL1 showed a more compact
633 architecture with distinct $CD20^+$ B-cell and $CD3^+$ T-cell zones but no evidence of
634 germinal center formation. FL2 displayed well-formed follicular structures
635 characterized by a dense $CD20^+$ B-cell core surrounded by a $CD3^+$ T-cell area,
636 accompanied by a $CD21^+$ follicular dendritic cell (FDC) network and positive staining
637 for BCL6 and Ki67 within the germinal center, indicating active B-cell proliferation.
638 Based on TLS morphological patterns (Agg, FL1, FL2) and their spatial distribution,
639 a four-tier TLS-based TME classification system was established, comprising:
640 Structured (presence of iTLS), Excluded (lack of iTLSs and presence of mature TLSs
641 outside tumor region), Immature (absence of iTLSs and all pTLSs are immature), and
642 Desertic (no iTLSs or pTLSs at all) phenotypes.
643 For spatial proteomic and paired IMC analyses, one experienced pathologist first
644 annotated the tumor core, invasive margin, and paratumoral regions at the whole-slide
645 level to evaluate TLS distribution (Figure S2F). Because TLSs were most abundantly
646 localized within the invasive margin, all ROIs for spatial proteomics were
647 subsequently selected from this region. Within the invasive margin, ROIs were further
648 categorized into three subtypes according to histological features: Tumor & Stroma,
649 Immune Cell Infiltrated areas (with varying immune density but no TLS structure),
650 and TLS Region.
651
652 **Immunohistochemical Staining**
653 Automated immunohistochemistry (IHC) was performed on 4-μm FFPE sections
654 using the BOND RX system (Leica Biosystems). Following deparaffinization and
655 rehydration, antigen retrieval was performed in EDTA buffer (pH 9.0; Leica, cat#
656 AR9640) at 100°C for 20 min. Endogenous peroxidase activity was blocked with 3%
657 H_2O_2 before incubation with primary antibodies: anti-CD20 (1:200; Abcam ab955),
658 anti-CD21 (1:200; Abcam ab955), anti-CD3 (1:200; Abcam ab955), anti-BCL6
659 (1:200; Abcam ab955), anti-Ki-67 (1:200; Abcam ab955) for 20 min at 37°C.
660 Detection employed the BOND Polymer Refine Detection Kit (Leica, cat# DS9800)
661 with DAB chromogen development. Counterstaining with hematoxylin (Leica, cat#
662 CS700), dehydration, and mounting preceded whole-slide scanning (Pannoramic 250
663 Flash II, 20×).
664
665 **Sample Preparation and Proteomic Analysis**

666 FFPE tissue samples were processed through sequential dewaxing and protein
667 extraction steps prior to mass spectrometry analysis. Samples were initially
668 equilibrated at 37°C for 30 minutes, followed by two 10-minute heptane incubations
669 for paraffin removal. Gradual rehydration was achieved through a series of ethanol
670 washes (100%, 90%, and 75% ethanol, 5 minutes each). The dewaxed samples were
671 then transferred to PCT tubes containing 12.5 µL of 100 mM Tris-HCl buffer (pH 10)
672 and subjected to protein extraction at 95°C with constant agitation (600 rpm) for 30
673 minutes.
674 Protein samples underwent reduction and alkylation in 30 µL of lysis buffer (6 M urea,
675 2 M thiourea, 100 mM TEAB) supplemented with 5 µL of 200 mM TCEP and 2.5 µL
676 of 800 mM IAA using Pressure Cycling Technology (PCT). This process involved 90
677 cycles of alternating high (45,000 psi for 30 seconds) and ambient pressure at 30°C.
678 Following buffer dilution with 75 µL of 0.1 M TEAB, enzymatic digestion was
679 performed with trypsin (0.5 µg/µL) and Lys-C (0.25 µg/µL) under 20,000 psi pressure
680 through 120 cycles (50 seconds high pressure/10 seconds ambient pressure) at 30°C.
681 The digestion was terminated by acidification with 15 µL of 10% trifluoroacetic acid,
682 and the resulting peptides were desalted using SOLAµ SPE cartridges (Thermo Fisher
683 Scientific) after confirming sample pH between 2-3.
684 LC-MS/MS analysis was conducted on a Vanquish Neo UHPLC system coupled to an
685 Orbitrap Astral mass spectrometer (Thermo Scientific). Peptides were separated on a
686 reversed-phase analytical column (1.9 µm, 120 Å pore size, 150 mm length × 75 µm
687 inner diameter) using a 500 nL/min flow rate with a 19-minute gradient from 8% to
688 40% mobile phase B (0.1% formic acid in 80% acetonitrile). The mass spectrometer
689 operated in data-independent acquisition (DIA) mode with FAIMS voltage set to -42
690 V. Full scan MS spectra were acquired from 380-980 m/z at 240,000 resolutions,
691 while MS/MS spectra covered 150-2000 m/z with 25% collision energy. The analysis
692 employed 299 isolation windows (2 m/z width) with automatic gain control targets of
693 500% and maximum injection times of 3 ms for both MS1 and MS2 scans.
694 Mass spectrometry data were processed using DIA-NN software (version 1.8.1)
695 against the UniProt human reference proteome database (2023-07-25 release) with
696 match-between-runs enabled. Static modification was set for carbamidomethylated
697 cysteine residues, while methionine oxidation was specified as a variable modification.
698 All identifications were filtered at a 1% false discovery rate threshold to ensure data
699 quality.
700
701 **Random Forest Model Construction and Validation**
702 We employed the R package ranger to construct a random forest classification model
703 for predicting iTLS status ($iTLS^+$ vs. $iTLS^-$) based on proteomic profiles. The model
704 was trained on the discovery cohort (n = 214) and subsequently validated on an
705 independent cohort (n = 155).
706 To ensure robustness, we performed 10 independent training iterations, each
707 initialized with a distinct random seed. In each iteration, the discovery cohort was

708 randomly partitioned into training (75%) and internal testing (25%) subsets.
709 Hyperparameter optimization was conducted via 5-fold cross-validation using a grid
710 search strategy to identify the optimal model configuration. The best-performing
711 parameters from each iteration were used to train the final model, and its predictive
712 performance was evaluated on the held-out test subset using receiver operating
713 characteristic (ROC) analysis. The results from all 10 iterations were aggregated to
714 assess overall model stability and accuracy. The validated model was then applied to
715 the independent validation cohort (n = 155) to evaluate its generalizability. Input data
716 consisted of standardized proteomic expression matrices, with binary iTLS
717 classification as the outcome variable.
718
719 **Gene Set Enrichment Analysis and Gene Ontology analysis**
720 Gene Set Enrichment Analysis (GSEA) was performed using the hallmark gene sets
721 from the Molecular Signatures Database (MSigDB) to identify enriched biological
722 pathways across TLS molecular subtypes. The analysis was conducted with GSEA
723 software using 1000 gene set permutations with weighted enrichment statistic and
724 signal-to-noise ratio for gene ranking. Gene sets meeting significance thresholds of
725 false discovery rate (FDR) < 0.25 and nominal p-value < 0.05 were considered
726 statistically enriched. For single-sample GSEA (ssGSEA), we calculated enrichment
727 scores for each sample using the same hallmark gene set collection, which were
728 subsequently correlated with immune cell abundances and clinical parameters. The
729 gene signature used in this study was summarized in Table S3.
730 Gene Ontology (GO) analysis was performed to identify significantly overrepresented
731 biological processes, molecular functions, and cellular components. We applied
732 Benjamini-Hochberg correction with an adjusted p-value cutoff of 0.05 and required a
733 minimum of 5 differentially expressed genes per term. To reduce redundancy among
734 significant GO terms, semantic similarity analysis was performed. KEGG pathway
735 enrichment analysis was performed using the clusterProfiler R package (*20*), with
736 pathways considered significantly enriched at a false discovery rate (FDR) < 0.05.
737
738 **Immune Architecture Analysis**
739 Building on previously established methods (*21*), immune cell interactions were
740 analyzed using a k-nearest neighbor graph built with the *buildSpatialGraph* function
741 from the imcRtools package. The analysis pipeline comprised three key
742 computational steps: First, spatial graphs were constructed using the
743 buildSpatialGraph function. Cellular neighborhoods (CNs) were subsequently
744 identified through k-means clustering (k=20) based on both cellular phenotypes and
745 spatial relationships. Second, cell-cell interactions were quantified using an expanded
746 neighborhood graph (15 μm expansion radius) where physically contacting cells were
747 considered interacting partners. The testInteractions function (histcat method) was
748 implemented to calculate interaction frequencies between all possible cell type pairs.
749 For each cell subset A, we determined the number of adjacent subset B cells and

750 normalized this by the proportion of A cells having ≥1 B-type neighbor within each
751 region of interest (ROI). Statistical significance was assessed through 1,000
752 permutations of cell type labels while maintaining spatial structure, generating
753 empirical null distributions. Significant interactions (attraction or avoidance) were
754 defined as those exceeding the 95th or falling below the 5th percentile of the null
755 distribution, respectively. Third, minimum intercellular distances were computed
756 using the minDistToCells function to quantify spatial relationships between specific
757 immune subsets. Fourth, effective score was calculated by total counts of a specific
758 neighbor cell type which is aggregated from k-nearest neighbor matrix, and then
759 summarized by mean for each center cell type (*22*). All analyses were performed at
760 the ROI level, with results aggregated by spatial immune type for comprehensive
761 visualization.
762 Spatial context maps were generated using a custom analysis pipeline developed by
763 Garry P. Nolan's group(*14*). To assess CN–CN spatial associations, we adapted the
764 general framework used for cellular neighborhood identification with several key
765 modifications. For each cell, spatial windows were defined using the 100 nearest
766 neighbors to capture broader local tissue architecture. Within each window, we used
767 CN labels—rather than single-cell annotations—to quantify the composition.
768 Instead of clustering the windows, we determined the smallest combination of CNs
769 that collectively accounted for more than 85% of the cells within each window, which
770 we defined as the spatial context. This approach captured the dominant CN
771 interactions in each local area. All unique combinations were counted and aggregated
772 to construct spatial context maps.
773 In the resulting network graphs, each node represented a unique CN combination,
774 with color indicating the CN pairing and node size reflecting its relative frequency
775 across the tissue. Graph rows corresponded to the number of CNs forming the
776 dominant combination in a window: windows dominated by a single CN (>85%) were
777 placed in the first row; windows with two CNs contributing >85% were placed in the
778 second row; and those with three or more CNs in the third or higher rows.
779 The number of CNs per spatial context provided insight into underlying structural
780 biology. Single-CN dominance indicated spatial compartmentalization, reflecting
781 large regions with uniform CN composition. Conversely, combinations involving
782 three or more CNs reflected mixed immune environments. Of particular interest, two-
783 CN combinations making up ≥85% of a window suggested structured interfaces
784 between immune compartments that may underlie coordinated functional activity.
785
786 **Xenium In Situ Spatial Transcriptomic Analysis**
787 The Xenium In Situ platform (10x Genomics) was employed for high-resolution
788 spatial transcriptomic profiling using a fully integrated system with automated sample
789 handling, liquid processing, and wide-field epifluorescence imaging capabilities. The
790 instrument features a dual-slide configuration with an imaging area of 12 × 24 mm
791 per slide and incorporates an optimized analytical pipeline performing image

792 preprocessing, fluorescent puncta detection, transcript decoding with quality score
793 assignment, and nuclear segmentation based on DAPI staining followed by
794 cytoplasmic expansion to a 15 μm radius or until adjacent cell boundary contact. The
795 platform generates standardized output files including feature-cell matrices in
796 HDF5/MEX formats compatible with 10x Genomics' single-cell RNA-seq pipelines,
797 transcript localization files containing mRNA coordinates and quality metrics, and
798 CSV-formatted cellular boundary definitions. For region-specific analysis, tissue
799 domains of interest were manually annotated using the polygon annotation tool in
800 Xenium Explorer software (10x Genomics developmental version), with coordinate
801 data exported in CSV format for subsequent computational integration, enabling
802 precise interrogation of transcriptomic patterns within histologically defined tissue
803 compartments.
804 Niche analysis is based on the BuildNicheAssay function from within Seurat to
805 construct a new assay called niche, which contains the cell type composition spatially
806 neighboring each cell. Due to the multiple fovs in our Xenium data, we first calculate
807 the 25 nearest neighbors in each fov separately and then merge the matrix together for
808 k-means clustering (k = 14).
809 For network visualization, the minimum distance between each cell type/niche was
810 computed and visualized using the R package qgraph (*23*). Frequency of each cell
811 type/niche was calculated for node size, and cellular/niche neighborhood (k = 25) was
812 aggregated for edge width.
813
814 **TLS states identification in Xenium**
815 A total of 61 TLS structures was first identified in the Xenium explorer software
816 regarding on both histological and molecular features. Pseudo-bulk expression matrix
817 for each TLS was generated from AggregateExpression function from Seurat package.
818 Inspired by previously established methods(*24*), we first performed PCA of TLSs in
819 each sample separately. TLSs in 4647T samples shows largest diversity among all
820 samples. Depended on this, we set TLSs from 4647T as a reference and projected
821 TLSs from other samples onto the 4647T's low-dimension space. Expression level of
822 representative gene including CXCL12, CXCL13, BANK1, CR2, RORC, and IRF8
823 were characterized. To classify TLSs into different states, we performed k-means
824 clustering on TLSs using the first two principal components (PC1 and PC2) with k set
825 to 3. Together with cell type components, we defined three pseudo-temporal TLS
826 states: Aggregated, Activated, and Post-activated. The cluster with a high LTi
827 signature (RORC) represented the early aggregated state. The cluster with high
828 expression of functional chemokines (CXCL13) and germinal center relative gene
829 (CR2) refers to the activated TLS state. The last cluster with descending chemokine
830 expression and increasing hypoxia signature were considered as post-activated TLS.
831
832 **Single-nucleus RNA Sequencing from FFPE Tissue**

833 FFPE tissue curls (50 μm) were dissociated using Liberase™ TH Research Grade
834 (Roche Diagnostics Deutschland GmbH, Cat# 05401151001) following the
835 manufacturer's protocol. The resulting nuclei were washed, counted, and resuspended,
836 and approximately 16,000 nuclei were loaded per well on a Chromium Chip Q (10x
837 Genomics), targeting a recovery of ~10,000 nuclei per GEM well.
838 Library preparation was performed using the Chromium Fixed RNA Profiling Kit
839 (10x Genomics, Cat# 1000474) according to the manufacturer's instructions.
840 Sequencing was carried out on an Illumina NovaSeq™ X Plus system using paired-
841 end dual indexing. Raw BCL files were demultiplexed using bcl2fastq (Illumina), and
842 the resulting FASTQ files were processed with Cell Ranger v7.0.1 (10x Genomics)
843 using the multi pipeline and aligned to the GRCh38-2020-A human reference genome.
844 Quality control and integration were performed using the "Seurat" R package (version
845 4.4.0) (*25*). To remove low-quality data, genes expressed in fewer than three cells
846 were excluded. Cells with fewer than 200 or more than 4,000 detected genes, were
847 filtered out to eliminate barcodes corresponding to empty droplets or potential
848 doublets. Cells with mitochondrial gene content exceeding 15% were also excluded.
849 Doublets and multiplets were identified and removed using the scDblFinder algorithm
850 with default parameters (*26*).
851 For data integration across individuals, Seurat's *IntegrateData* function was applied
852 to correct for batch effects and project all single cells into a shared low-dimensional
853 space. After integration, a graph-based unsupervised clustering algorithm was
854 implemented using Seurat's default pipeline. The UMI count matrix was first
855 normalized with the *NormalizeData* function, and log-normalized expression values
856 were used to identify 2,000 highly variable genes via the *FindVariableFeatures*
857 function with the "vst" method. These genes were then used for dimensionality
858 reduction by principal component analysis (PCA), with 20 PCs retained after
859 regressing out total UMI counts.
860 Clustering was performed on the top 20 PCs using the *FindClusters* function at a
861 resolution of 1.2. Clusters were visualized via Uniform Manifold Approximation and
862 Projection (UMAP) and annotated based on canonical lineage markers. To define
863 cluster-specific marker genes, the *FindAllMarkers* function was applied using the
864 Wilcoxon rank-sum test, with thresholds set to min.pct = 0.25 and logfc.threshold =
865 0.25. Identified marker genes, together with known lineage-specific signatures, were
866 used for downstream cluster annotation. The 10x flex sequencing data was spatially
867 mapped to 10x xenium data by Tangram package(*27*) at cluster level with default
868 parameters.
869
870 **Tissue Distribution of Clusters**
871 For each cell subtype, we evaluated its distribution pattern across the four groups
872 through the calculation of the Ro/e as previously described (*28*). Specifically, Ro/e is
873 the ratio of the observed cell number to the expected cell number of a given
874 combination of cell subtype and tissue. We used the "calTissueDist" function from

875 the Startrac package to obtain the observed and expected cell numbers, using cell
876 frequency as the input data. Briefly, a cell subtype was more frequently observed in a
877 specific tissue than random expectations when Ro/e >1 and was therefore assumed to
878 be enriched in that group.
879
880 **Statistical analysis**
881 All statistical analyses were performed using the R software (Version 4.4.1) and the
882 Python software (Version 3.12.7). The Cox proportional-hazards model was utilized
883 to compare the survival outcomes. Data are presented as mean ± standard deviation.
884 Statistical significance was determined as follows: *$p < 0.05$, **$p < 0.01$, ***$p <$
885 0.001.
886

887 **Reference**

888

889 1. F. Bray, M. Laversanne, H. Sung, J. Ferlay, R. L. Siegel, I. Soerjomataram, A.
890 Jemal, Global cancer statistics 2022: GLOBOCAN estimates of incidence and
891 mortality worldwide for 36 cancers in 185 countries. *CA: a cancer journal for*
892 *clinicians* **74**, 229-263 (2024).
893 2. D.-Y. Oh, A. R. He, M. Bouattour, T. Okusaka, S. Qin, L.-T. Chen, M. Kitano,
894 C.-k. Lee, J. W. Kim, M.-H. Chen, Durvalumab or placebo plus gemcitabine
895 and cisplatin in participants with advanced biliary tract cancer (TOPAZ-1):
896 updated overall survival from a randomised phase 3 study. *The Lancet*
897 *Gastroenterology & Hepatology* **9**, 694-704 (2024).
898 3. C. Sautès-Fridman, F. Petitprez, J. Calderaro, W. H. Fridman, Tertiary
899 lymphoid structures in the era of cancer immunotherapy. *Nature Reviews*
900 *Cancer* **19**, 307-325 (2019).
901 4. R. I. R. Macias, S. Roessler, M. M. A. Verstegen, Deciphering the spatial
902 tumor microenvironment in intrahepatic cholangiocarcinoma. *Hepatology*,
903 (2025).
904 5. L. Hong, J. Mei, X. Sun, Y. Wu, Z. Dong, Y. Jin, L. Gao, J. Cheng, W. Tian, C.
905 Liu, B. Li, P. Hu, L. Liu, S. Xin, X. Dai, P. Zhao, R. Guo, M. Chen, J. Yun, B.
906 Lin, W. Wei, W. Fang, X. Bao, Spatial single-cell proteomics landscape
907 decodes the tumor microenvironmental ecosystem of intrahepatic
908 cholangiocarcinoma. *Hepatology*, (2025).
909 6. Y. Zhang, G. Liu, Q. Zeng, W. Wu, K. Lei, C. Zhang, M. Tang, Y. Zhang, X.
910 Xiang, L. Tan, R. Cui, S. Qin, X. Song, C. Yin, Z. Chen, M. Kuang, CCL19-
911 producing fibroblasts promote tertiary lymphoid structure formation enhancing
912 anti-tumor IgG response in colorectal cancer liver metastasis. *Cancer Cell* **42**,
913 1370-1385 e1379 (2024).
914 7. J. Calderaro, F. Petitprez, E. Becht, A. Laurent, T. Z. Hirsch, B. Rousseau, A.
915 Luciani, G. Amaddeo, J. Derman, C. Charpy, J. Zucman-Rossi, W. H. Fridman,
916 C. Sautes-Fridman, Intra-tumoral tertiary lymphoid structures are associated
917 with a low risk of early recurrence of hepatocellular carcinoma. *J Hepatol* **70**,
918 58-65 (2019).
919 8. D. H. Shu, W. J. Ho, L. T. Kagohara, A. Girgis, S. M. Shin, L. Danilova, J. W.
920 Lee, D. N. Sidiropoulos, S. Mitchell, K. Munjal, K. Howe, K. J. Bendinelli, E.
921 Kartalia, H. Qi, G. Mo, J. Montagne, J. M. Leatherman, T. Y. Lopez-Vidal, Q.
922 Zhu, A. L. Huff, X. Yuan, A. Hernandez, E. M. Coyne, N. Zaidi, D. J.
923 Zabransky, L. L. Engle, A. Ogurtsova, M. Baretti, D. Laheru, J. N. Durham, H.
924 Wang, J. C. Sunshine, R. J. Johnston, J. S. Deutsch, J. M. Taube, R. A.
925 Anders, E. M. Jaffee, E. J. Fertig, M. Yarchoan, Immunotherapy response
926 induces divergent tertiary lymphoid structure morphologies in hepatocellular
927 carcinoma. *Nat Immunol* **25**, 2110-2123 (2024).
928 9. G.-Y. Ding, J.-Q. Ma, J.-P. Yun, X. Chen, Y. Ling, S. Zhang, J.-Y. Shi, Y.-Q.

Chang, Y. Ji, X.-Y. Wang, Distribution and density of tertiary lymphoid structures predict clinical outcome in intrahepatic cholangiocarcinoma. *Journal of Hepatology* **76**, 608-618 (2022).

10. Z. Tang, Y. Bai, Q. Fang, Y. Yuan, Q. Zeng, S. Chen, T. Xu, J. Chen, L. Tan, C. Wang, Q. Li, J. Lin, Z. Yang, X. Wu, G. Shi, J. Wang, C. Yin, J. Guo, S. Liu, S. Peng, M. Kuang, Spatial transcriptomics reveals tryptophan metabolism restricting maturation of intratumoral tertiary lymphoid structures. *Cancer Cell* **43**, 1025-1044.e1014 (2025).
11. I. P. MacFawn, G. Magnon, G. Gorecki, S. Kunning, R. Rashid, M. E. Kaiza, H. Atiya, A. T. Ruffin, S. Taylor, T. R. Soong, The activity of tertiary lymphoid structures in high grade serous ovarian cancer is governed by site, stroma, and cellular interactions. *Cancer Cell* **42**, 1864-1881. e1865 (2024).
12. M.-C. Dieu-Nosjean, J. Goc, N. A. Giraldo, C. Sautès-Fridman, W. H. Fridman, Tertiary lymphoid structures in cancer and beyond. *Trends in immunology* **35**, 571-580 (2014).
13. J. W. Hickey, M. Haist, N. Horowitz, C. Caraccio, Y. Tan, A. J. Rech, M. A. Baertsch, X. Rovira-Clave, B. Zhu, G. Vazquez, G. Barlow, E. Agmon, Y. Goltsev, J. B. Sunwoo, M. Covert, G. P. Nolan, T cell-mediated curation and restructuring of tumor tissue coordinates an effective immune response. *Cell Rep* **42**, 113494 (2023).
14. S. S. Bhate, G. L. Barlow, C. M. Schurch, G. P. Nolan, Tissue schematics map the specialization of immune tissue motifs and their appropriation by tumors. *Cell Syst* **13**, 109-130 e106 (2022).
15. M. Ukita, J. Hamanishi, H. Yoshitomi, K. Yamanoi, S. Takamatsu, A. Ueda, H. Suzuki, Y. Hosoe, Y. Furutake, M. Taki, CXCL13-producing CD4+ T cells accumulate in the early phase of tertiary lymphoid structures in ovarian cancer. *JCI insight* **7**, e157215 (2022).
16. E. M. Pimenta, B. J. Barnes, Role of tertiary lymphoid structures (TLS) in anti-tumor immunity: potential tumor-induced cytokines/chemokines that regulate TLS formation in epithelial-derived cancers. *Cancers* **6**, 969-997 (2014).
17. W. H. Fridman, M. Meylan, F. Petitprez, C.-M. Sun, A. Italiano, C. Sautès-Fridman, B cells and tertiary lymphoid structures as determinants of tumour immune contexture and clinical outcome. *Nature reviews Clinical oncology* **19**, 441-457 (2022).
18. W. H. Fridman, M. Meylan, G. Pupier, A. Calvez, I. Hernandez, C. Sautès-Fridman, Tertiary lymphoid structures and B cells: An intratumoral immunity cycle. *Immunity* **56**, 2254-2269 (2023).
19. M. Meylan, F. Petitprez, E. Becht, A. Bougouin, G. Pupier, A. Calvez, I. Giglioli, V. Verkarre, G. Lacroix, J. Verneau, C. M. Sun, P. Laurent-Puig, Y. A. Vano, R. Elaidi, A. Mejean, R. Sanchez-Salas, E. Barret, X. Cathelineau, S. Oudard, C. A. Reynaud, A. de Reynies, C. Sautes-Fridman, W. H. Fridman, Tertiary lymphoid structures generate and propagate anti-tumor antibody-producing

plasma cells in renal cell cancer. *Immunity* **55**, 527-541 e525 (2022).

20. G. Yu, L.-G. Wang, Y. Han, Q.-Y. He, clusterProfiler: an R package for comparing biological themes among gene clusters. *Omics: a journal of integrative biology* **16**, 284-287 (2012).
21. H. Salié, L. Wischer, A. D'Alessio, I. Godbole, Y. Suo, P. Otto-Mora, J. Beck, O. Neumann, A. Stenzinger, P. Schirmacher, C. A. M. Fulgenzi, A. Blaumeiser, M. Boerries, N. Roehlen, M. Schultheiß, M. Hofmann, R. Thimme, D. J. Pinato, T. Longerich, B. Bengsch, Spatial single-cell profiling and neighbourhood analysis reveal the determinants of immune architecture connected to checkpoint inhibitor therapy outcome in hepatocellular carcinoma. *Gut* **74**, 451-466 (2025).
22. Y. Chen, K. Jia, Y. Sun, C. Zhang, Y. Li, L. Zhang, Z. Chen, J. Zhang, Y. Hu, J. Yuan, Predicting response to immunotherapy in gastric cancer via multi-dimensional analyses of the tumour immune microenvironment. *Nature communications* **13**, 4851 (2022).
23. S. Epskamp, A. O. J. Cramer, L. J. Waldorp, V. D. Schmittmann, D. Borsboom, qgraph: Network Visualizations of Relationships in Psychometric Data. *Journal of Statistical Software* **48**, 1 - 18 (2012).
24. Y. Yan, D. Sun, J. Hu, Y. Chen, L. Sun, H. Yu, Y. Xiong, Z. Huang, H. Xia, X. Zhu, D. Bian, F. Sun, L. Hou, C. Wu, O. R. Fan, H. Hu, A. Zeng, L. Zhang, Y. E. Sun, C. Wang, P. Zhang, Multi-omic profiling highlights factors associated with resistance to immuno-chemotherapy in non-small-cell lung cancer. *Nat Genet* **57**, 126-139 (2025).
25. F. A. Wolf, P. Angerer, F. J. Theis, SCANPY: large-scale single-cell gene expression data analysis. *Genome Biol* **19**, 15 (2018).
26. P. L. Germain, A. Lun, C. Garcia Meixide, W. Macnair, M. D. Robinson, Doublet identification in single-cell sequencing data using scDblFinder. *F1000Res* **10**, 979 (2021).
27. T. Biancalani, G. Scalia, L. Buffoni, R. Avasthi, Z. Lu, A. Sanger, N. Tokcan, C. R. Vanderburg, Å. Segerstolpe, M. Zhang, Deep learning and alignment of spatially resolved single-cell transcriptomes with Tangram. *Nature methods* **18**, 1352-1362 (2021).
28. Y. Chen, D. Wang, Y. Li, L. Qi, W. Si, Y. Bo, X. Chen, Z. Ye, H. Fan, B. Liu, Spatiotemporal single-cell analysis decodes cellular dynamics underlying different responses to immunotherapy in colorectal cancer. *Cancer Cell* **42**, 1268-1285. e1267 (2024).

Acknowledgements

This work was supported in part by the National Natural Science Foundation of China 82473471, 82102817, 82373428 and by Zhejiang Provincial National Science Foundation of China LY23H160013 and by the Major Scientific Project of Zhejiang Province 2023C03061 and by the "Pioneer" and "Leading Goose" R&D Program of Zhejiang Province 2023C03061 and 2025C02073. We give thanks for technical support by the Central Laboratory (Zhi Jiang Division), the First Affiliated Hospital, School of Medicine, Zhejiang University.

Declaration of interests

The authors declare no competing interests.

Author contributions

Writing - original draft: Liaoliao Gao, Jie Mei, Xuanwen Bao. Writing - review & editing: Liaoliao Gao, Libing Hong, Yuzhi Jin, Xuqi Sun, Chuan Liu, Bin Li, Xiaomeng Dai, Bo Lin, Yajie Sun, Peng Zhao, Minshan Chen, Rongping Guo, Shan Xin, Jingping Yun, Inmaculada Reyes, Weijia Fang, Xuanwen Bao. Conceptualization: Liaoliao Gao, Jie Mei, Shan Xin, Wei Wei, Weijia Fang, Xuanwen Bao. Investigation: Liaoliao Gao, Jinlin Cheng, Xuanwen Bao. Methodology: Liaoliao Gao, Jie Mei, Wei Wei, Weijia Fang, Xuanwen Bao. Resources: Liaoliao Gao, Weijia Fang, Xuanwen Bao. Data curation: Liaoliao Gao, Jie Mei, Libing Hong. Formal analysis: Liaoliao Gao, Libing Hong, Yuzhi Jin, Jinlin Cheng. Software: Liaoliao Gao, Jie Mei. Visualization: Liaoliao Gao, Libing Hong, Yuzhi Jin, Xuqi Sun. Validation: Liaoliao Gao, Xuanwen Bao. Supervision: Wei Wei, Weijia Fang, Xuanwen Bao. Project administration: Weijia Fang, Xuanwen Bao. Funding acquisition: Jie Mei, Xiaomeng Dai, Weijia Fang, Xuanwen Bao.

Data availability

The proteomics data of the discovery cohort have been deposited in the iProX under the project number IPX0011444000. The snRNA-seq data and Xenium spatial transcriptomics data have been deposited in the National Genomics Data Center (NGDC) database under the accession numbers HRA012124 and OMIX012686, respectively. Publicly available datasets used in this study can be accessed from the Gene Expression Omnibus (GEO) under accession numbers GSE91061 and GSE126044, and from the European Nucleotide Archive (ENA) under accession number PRJEB23709.

1043 **Figure**

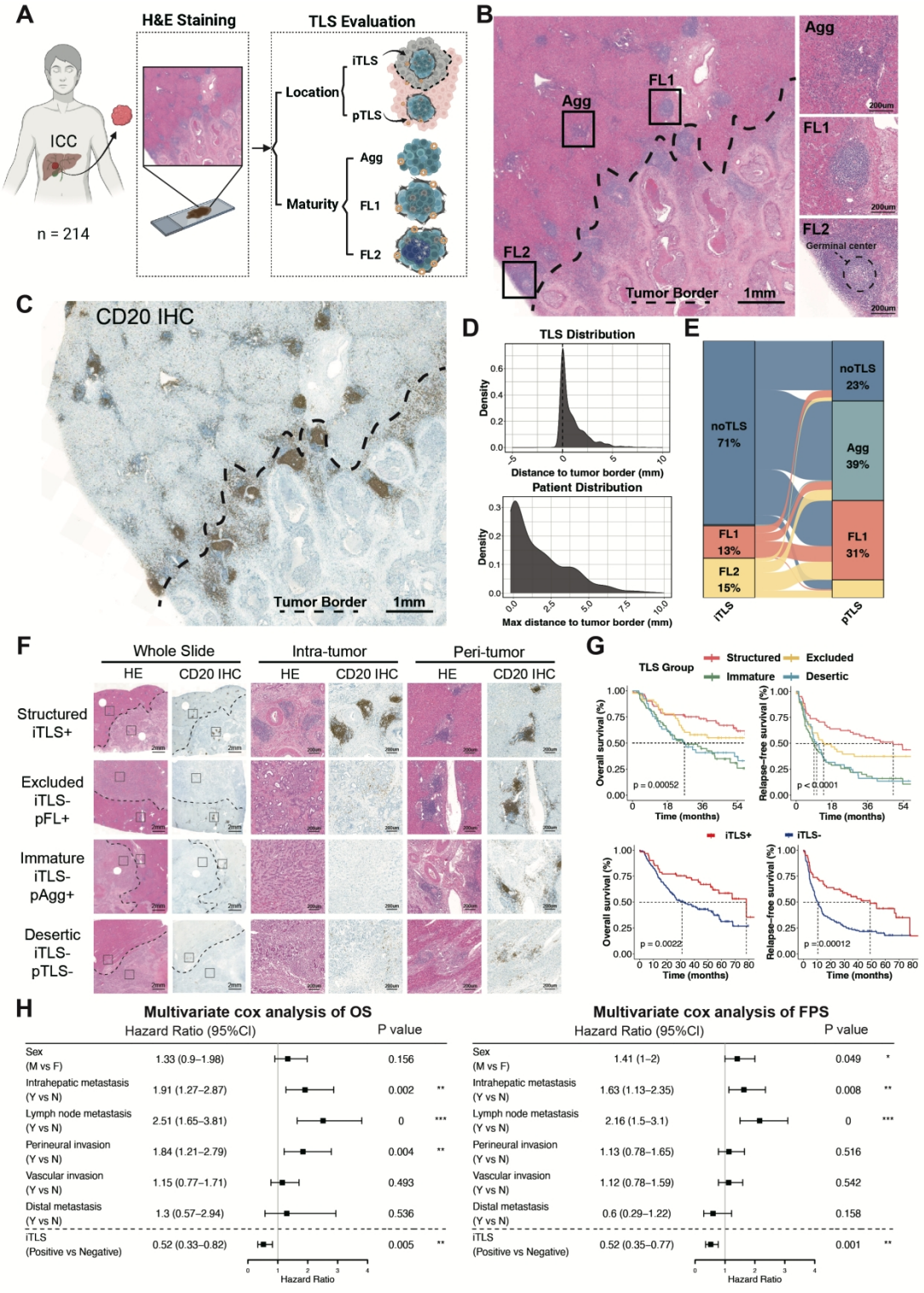

1044

1045 **Figure 1. Comprehensive evaluation of TLS distribution, morphology, and**
1046 **prognostic classification in iCCA.**
1047 (A) Schematic overview of TLS identification, spatial annotation, morphological
1048 classification, and prognostic stratification in intrahepatic cholangiocarcinoma (iCCA).

(B) Representative hematoxylin and eosin (H&E) stained images showing the three morphological subtypes of tertiary lymphoid structures (TLS): lymphoid aggregates (AGG), primary follicles (FL1), and secondary follicles (FL2).

(C) Representative immunohistochemical staining of CD20 highlighting B-cell-rich TLS structures, supporting morphological classification.

(D) Density plot showing the spatial distribution of TLS relative to the tumor boundary, demonstrating predominant localization within 5 mm from the tumor edge.

(E) Sankey diagram depicting patient-level TLS maturation patterns across intra-tumoral and peri-tumoral compartments. Each patient was assigned a TLS status for both regions based on the most advanced morphology observed (hierarchy: FL2 > FL1 > Agg > none).

(F) Histological and immunohistochemical images (H&E and CD20 staining) demonstrating the criteria used to define the four-tier TLS classification: Structured (mature intratumoral TLS), Excluded (iTLS– & pFL+), Immature (iTLS– & pAGG+), and Desertic (iTLS– & pTLS–).

(G) Kaplan–Meier survival curves showing overall survival (OS) and progression-free survival (PFS) across TME subtypes, indicating significant prognostic stratification.

(H) Forest plots from multivariate Cox regression analysis demonstrating iTLS presence as an independent prognostic factor for both OS and PFS.

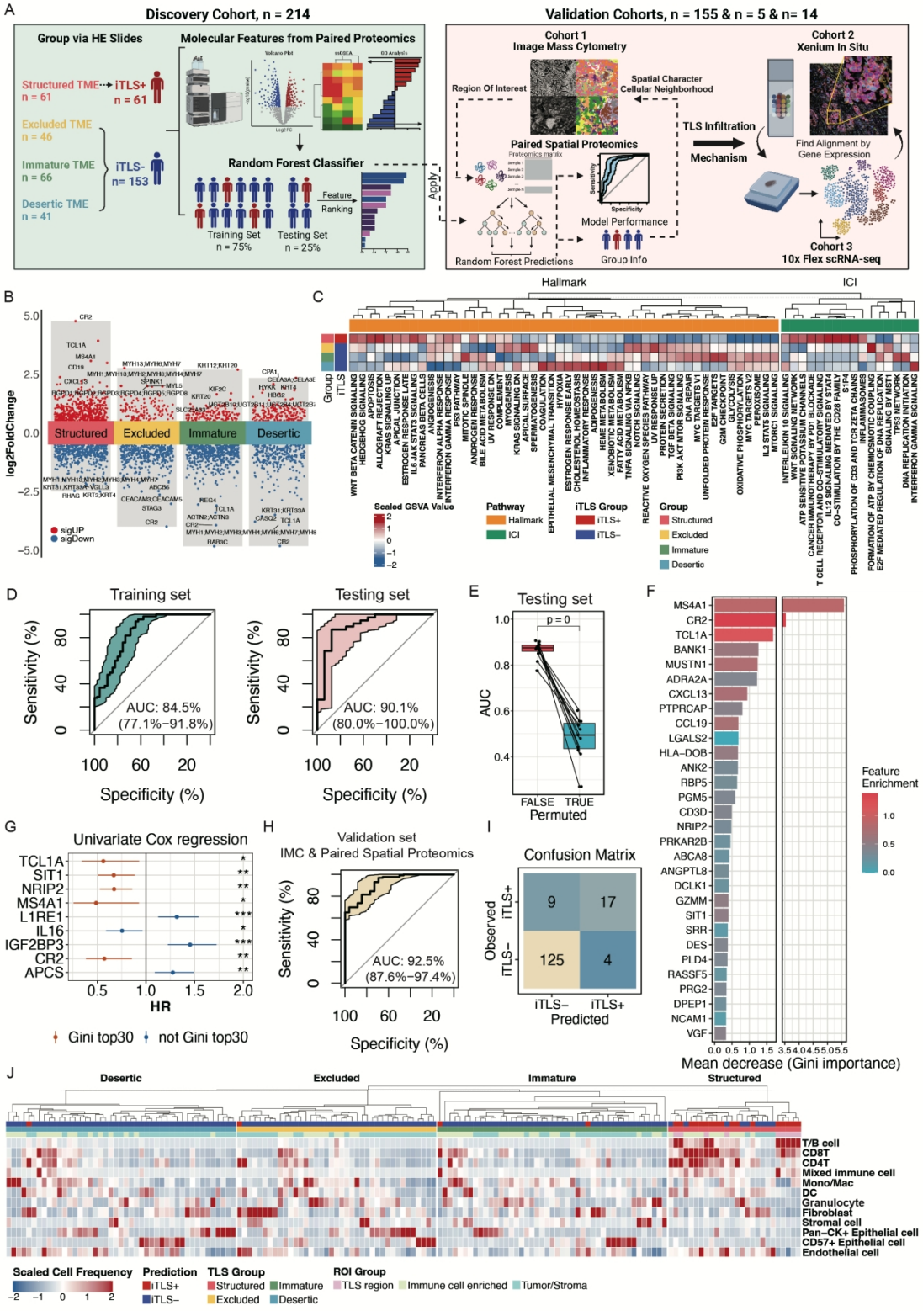

Figure 2. Proteomic and spatial characterization of TLS-associated tumor microenvironment subtypes in iCCA.

(A) Overview of the integrated spatial multi-omics strategy used to characterize TLS heterogeneity in iCCA, including bulk proteomics, imaging mass cytometry (IMC),

single-nucleus RNA sequencing (snRNA-seq), and spatial transcriptomics (10x Xenium).

(B) Volcano plot showing differentially expressed proteins between TME subtypes identified in the discovery cohort (n = 214). Notably, Structured tumors show upregulation of lymphoid markers such as CR2, CD19, MS4A1, and CXCL13, while Desertic tumors upregulate epithelial programs (e.g., KRT4).

(C) Heatmap of pathway enrichment scores reveals immunoactive signaling in Structured subtype (e.g., CD28 co-stimulation, S1PR4, IL-12 response) and hypoxia/EMT/coagulation programs in Desertic subtype.

(D) Performance of the TME subtype prediction model using a random forest classifier trained on proteomic data, showing training and testing AUCs (84.5% and 90.1%, respectively; $p < 0.001$).

(E) Boxplot comparing AUC values of the random forest model in the testing cohort under true versus permuted TLS labels, demonstrating significant performance drop in permuted conditions and confirming the model's specificity.

(F) Feature importance analysis from the random forest model, highlighting top discriminative proteins including MS4A1, CR2, TCL1A, BANK1, MUSTN1, ADRA2A, and CXCL13.

(G) Univariate survival analysis of the top-ranked features and others from TLS-prediction model, showing significant prognostic associations.

(H) ROC curve demonstrating external validation performance of the TLS prediction model in an independent iCCA cohort (n = 155) using expansion-gel-based spatial proteomics (AUC = 92.5%).

(I) Confusion matrix evaluating prediction accuracy in the validation cohort, confirming high classification performance.

(J) Heatmap generated from IMC data showing cellular composition and spatial immune architecture across TME subtypes. Structured tumors feature dense, organized lymphoid aggregates; Excluded and Immature subtypes display compartmentalized immune patterns; Desertic tumors exhibit immune-depleted, stromal-dominant landscapes.

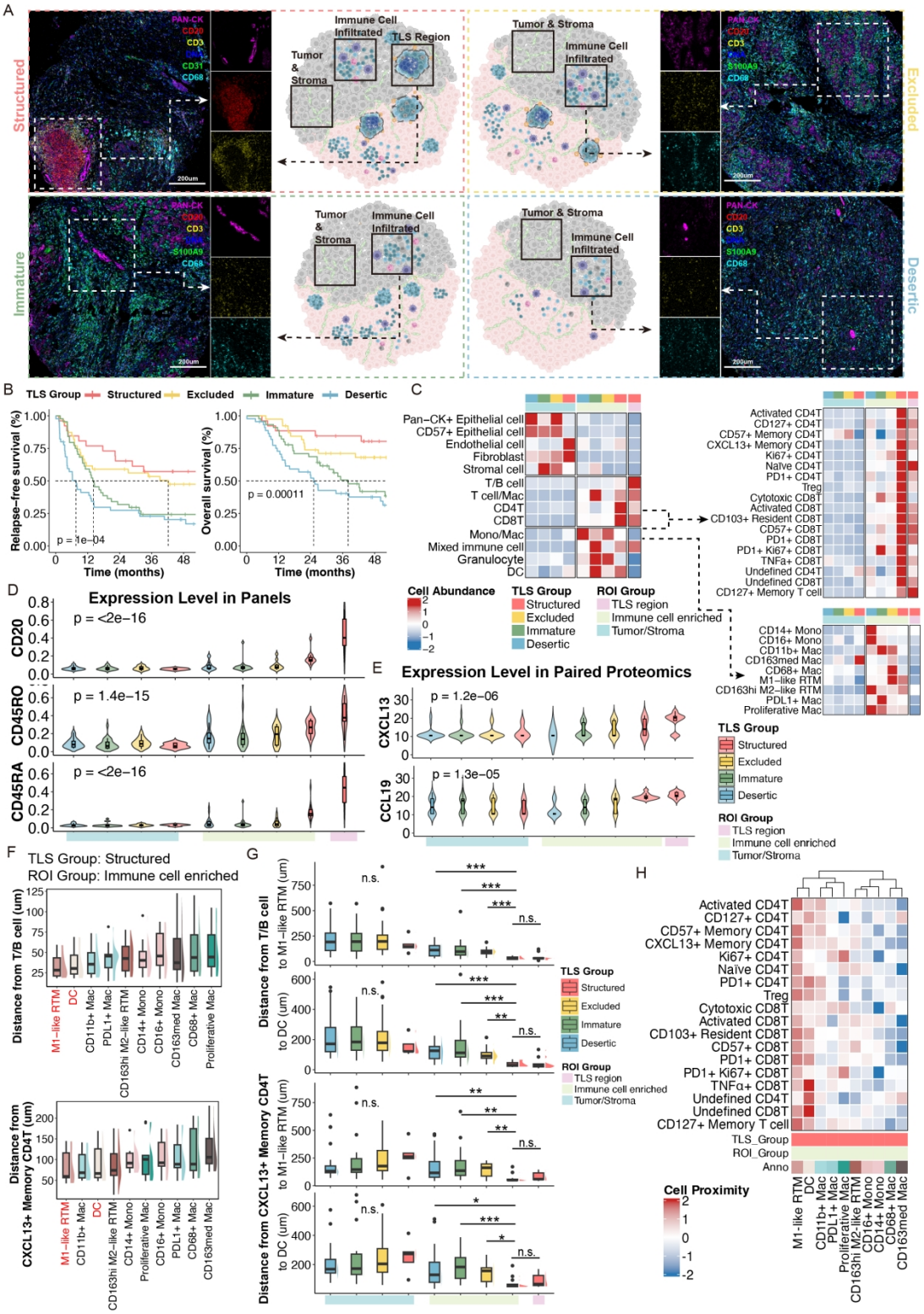

Figure 3. Single-cell spatial architecture of TLS-enriched tumor microenvironments in iCCA.

(A) Workflow of imaging mass cytometry (IMC) analysis with region-of-interest (ROI) segmentation in TLS, immune-infiltrated, and tumor/stroma regions across iCCA samples.

(B) Kaplan-Meier survival analysis in the validation cohort showing significantly improved overall survival across TME subtypes (p = 1e-04) and between iTLS^{+} and iTLS^{-} groups (p = 0.00011).

(C) Heatmap displaying the relative abundance of immune cell subsets across spatial compartments. Structured TLS regions are enriched for CXCL13^{+} TFH-like memory CD4^{+} T cells, naïve CD4^{+} T cells, PD-1^{+} CD4^{+} T cells, and CD20^{+} B cells.

(D) Boxplots showing IMC-derived expression levels of key markers (CD20, CD45RO, CD45RA), revealing spatial gradients with highest expression in TLS regions.

(E) Violinplot of expansion-gel based spatial proteomics data demonstrating compartment-specific expression of TLS-associated chemokines (CXCL13, CCL19), with enrichment in TLS regions.

(F) Boxplots quantifying mean spatial distances between M1-like resident tissue macrophages (RTMs) and lymphoid cells (T/B cells and CXCL13^{+} CD4^{+} T cells), highlighting their close physical proximity in TLS regions.

(G) Boxplots quantifying distances from T/B cells and CXCL13^{+} CD4^{+} T cells to RTMs and DCs across spatial compartments. A consistent decrease in distance is observed from tumor/stroma to immune-infiltrated zones and further into TLS regions, reflecting increasing spatial organization of immune cell interactions during TLS maturation.

(H) Heatmap of pairwise spatial proximities between myeloid populations and CD4^{+} T cell subsets. M1-like RTMs show preferential interactions with CXCL13^{+} memory CD4^{+} T cells, supporting their role as structural anchors in TLS organization.

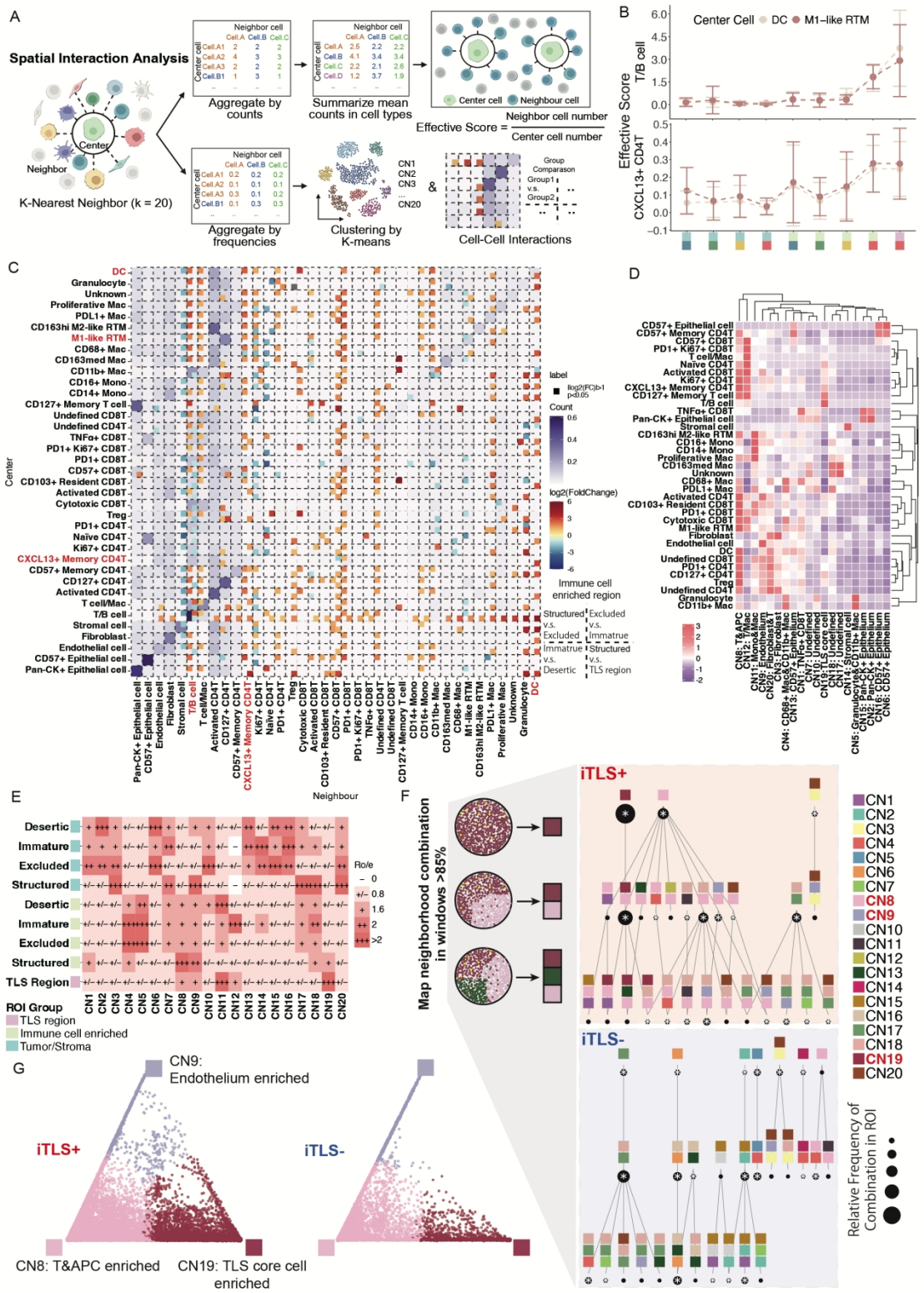

Figure 4. Spatial interaction networks define TLS-associated cellular neighborhoods in iCCA.

(A) Schematic workflow for multi-layered spatial analysis integrating Effective Score (ES), pairwise cell interaction (PCI), and cellular neighborhood (CN) profiling.

1137 (B) Boxplots showing ES values of M1-like RTMs and DCs across tissue regions,
1138 highlighting selective enrichment in TLS regions of structured subtype tumor.
1139 (C) Heatmap comparing spatial distances between M1-like RTMs or DCs and
1140 $CXCL13^+$ $CD4^+$ T cells or T/B cell clusters across subtypes. M1-like RTMs and DCs
1141 exhibit the shortest interaction distances in structured TLS^+ tumors.
1142 (D) Heatmap depicting relative abundance of major immune cell types across distinct
1143 CNs.
1144 (E) RO/e analysis showing spatial distribution of CN8 and CN19 across tissue
1145 compartments. CN19 is enriched in TLS regions of structured subtype, while CN8
1146 localizes to immune cell-enriched regions of structured subtype.
1147 (F) CN interaction analysis illustrating stronger CN8–CN19-CN9 interactions in TLS^+
1148 tumors, particularly in the structured subtype.
1149 (G) Triangle plot demonstrating increased co-occurrence of CN8, CN19, and CN9 in
1150 TLS^+ tumors, reflecting coordinated spatial coupling within mature TLS regions.

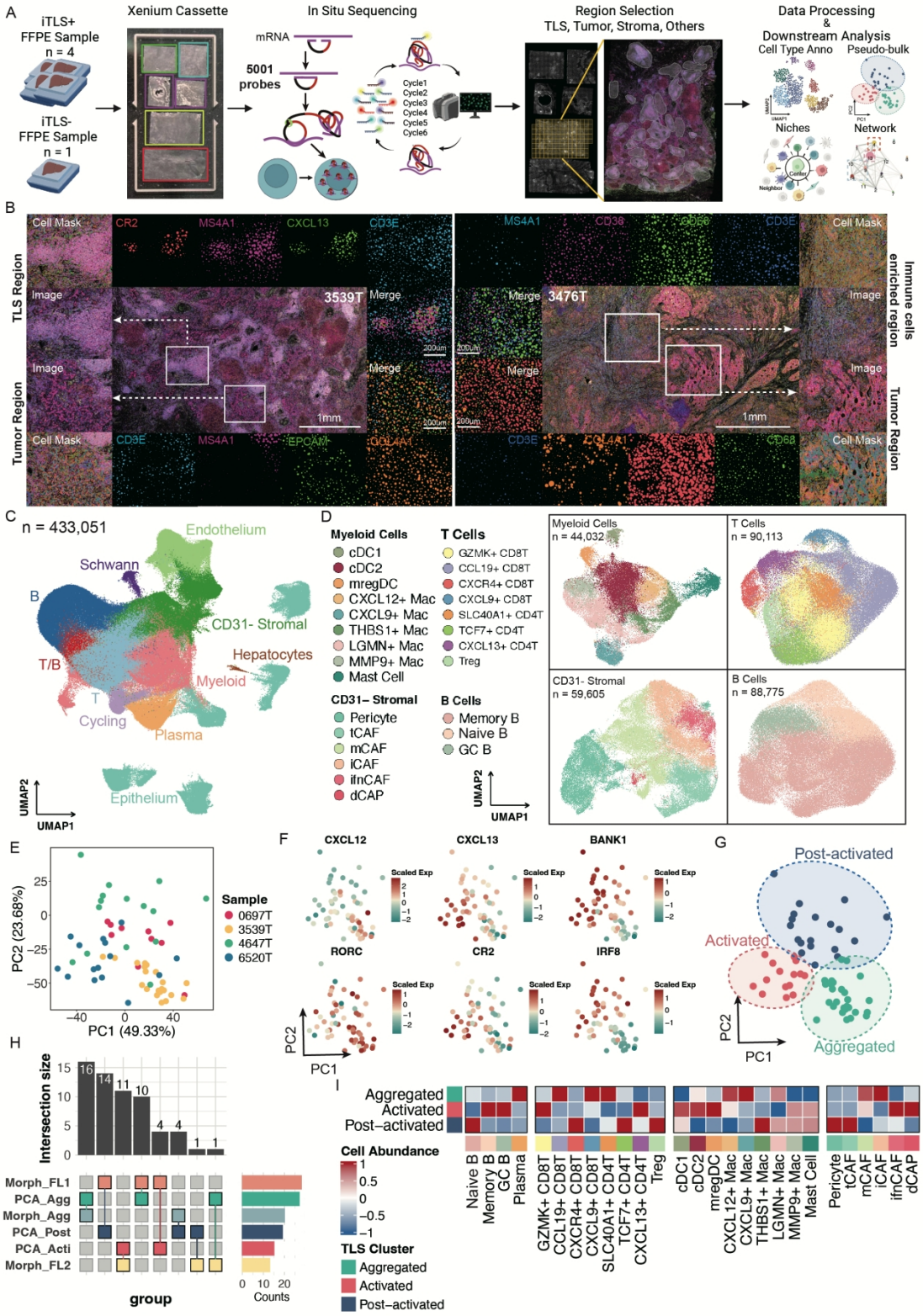

Figure 5. Single-cell spatial transcriptomics reveals TLS molecular heterogeneity and pseudo-temporal subtypes.

(A) Schematic overview of the 10x Xenium spatial transcriptomics workflow for profiling TLS at single-cell resolution in iCCA.

1156 (B) Representative spatial transcriptomic images from iTLS^{+} and iTLS^{-} samples,
1157 showing TLS detection and localization.
1158 (C) UMAP embedding of all 433,051 spatially resolved cells colored by major
1159 immune and stromal lineages.
1160 (D) Sub-UMAPs showing detailed annotation of myeloid cells, T cells, stromal cells,
1161 and B cells.
1162 (E) Pseudo-bulk PCA treating each of the 61 identified TLS as an individual unit;
1163 each dot represents a TLS, colored by patient/sample identity.
1164 (F) PCA of TLS colored by expression levels of selected TLS-related markers (e.g.,
1165 CXCL13, CXCL12, BANK1, RORC, CR2, IRF8), used to define pseudo-temporal
1166 states.
1167 (G) Pseudo-temporal classification of TLS into three molecular subtypes: Aggregated,
1168 Activated, and Post-activated.
1169 (H) UpSet plot showing the overlap between molecular subtypes and morphological
1170 subtypes (AGG, FL1, FL2), revealing partial concordance but substantial
1171 heterogeneity within each morphological class.
1172 (I) Heatmap showing differences in cellular composition among TLS molecular
1173 subtypes, with Aggregated TLS enriched in plasma cells, Activated TLS enriched in
1174 CXCL13^{+} CD4^{+} T cells, and Post-activated TLS enriched in TCF7^{+} CD4^{+} T cells and
1175 Tregs.

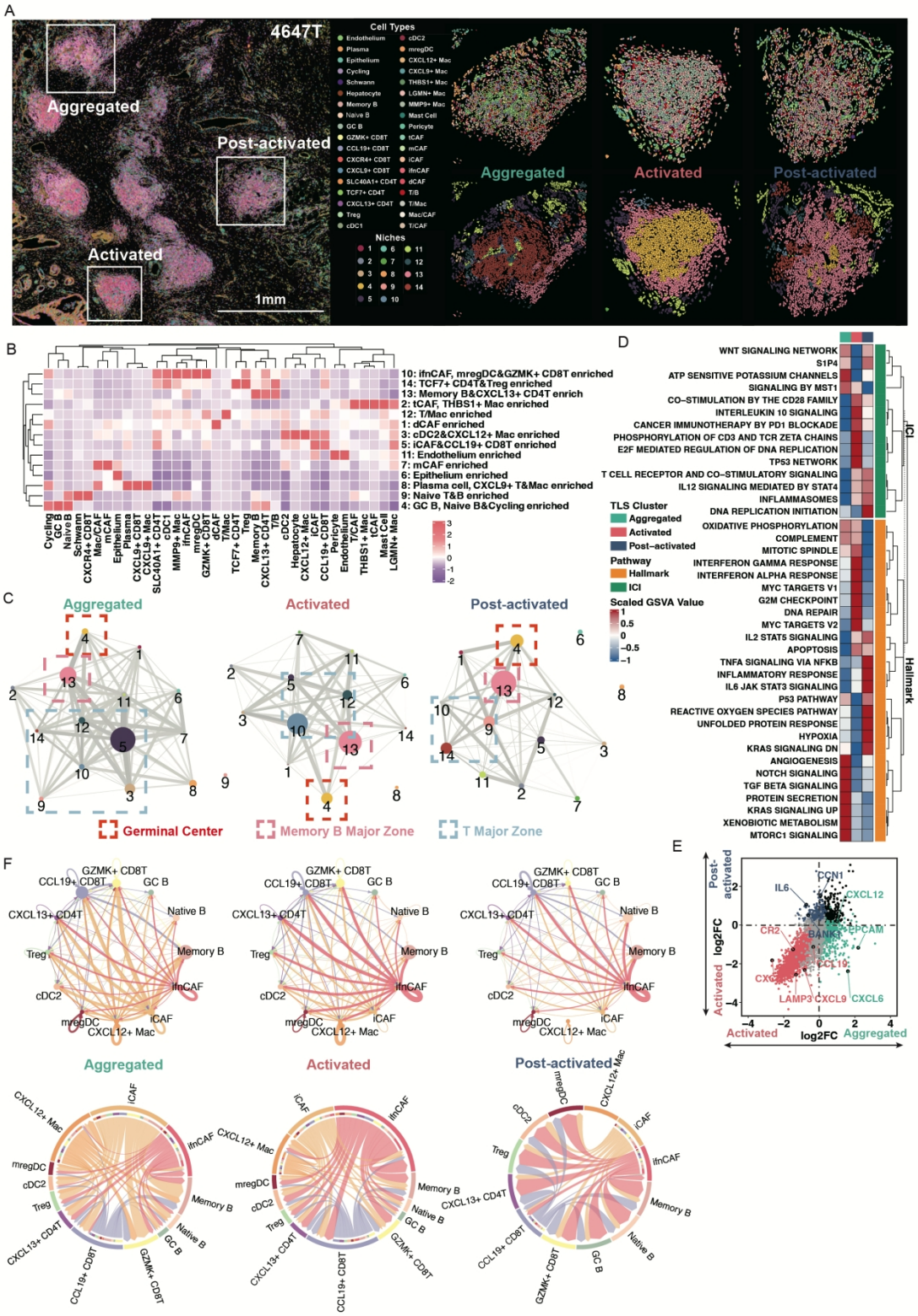

Figure 6. Pseudo-temporal spatial niche remodeling and intercellular signaling across TLS maturation states in iCCA.

(A) Schematic of spatial niche analysis across three TLS molecular states (Aggregated, Activated, Post-activated) based on single-cell spatial transcriptomic data.

(B) Heatmap displaying the cellular composition of 14 spatial niches, with each niche characterized by specific enrichment of stromal, myeloid, and lymphoid cell subsets.
(C) Niche interaction networks reconstructed separately for Aggregated, Activated, and Post-activated TLS, revealing stage-specific topologies. Aggregated TLS show sparse stromal-lymphoid connectivity; Activated TLS exhibit expanded immune coordination; Post-activated TLS display dense regulatory niche interactions.
(D) Heatmap of single-sample GSEA (ssGSEA) scores demonstrating hallmark and immune checkpoint-related pathway activities across TLS states. Activated TLS show enrichment for IFN-γ and antigen presentation pathways, while Post-activated TLS are enriched for Treg and immune regulatory signatures.
(E) Volcano plot showing differentially expressed genes across TLS molecular states, highlighting key immune regulators and TLS-related chemokines (e.g., CXCL12, IL6, LAMP3, CR2).
(F) Intercellular communication networks and CXCL12 signaling dynamics during TLS maturation. Top panels: Niche-specific communication networks in Aggregated (left), Activated (middle), and Post-activated (right) TLS subtypes, showing dominant cell-cell interactions (edges) and key signaling cell populations (nodes). Bottom panels: Corresponding CXCL12 signaling pathways across maturation stages, illustrating dynamic changes in signal-sending cell types (colored nodes) and interaction strengths (edge weights).

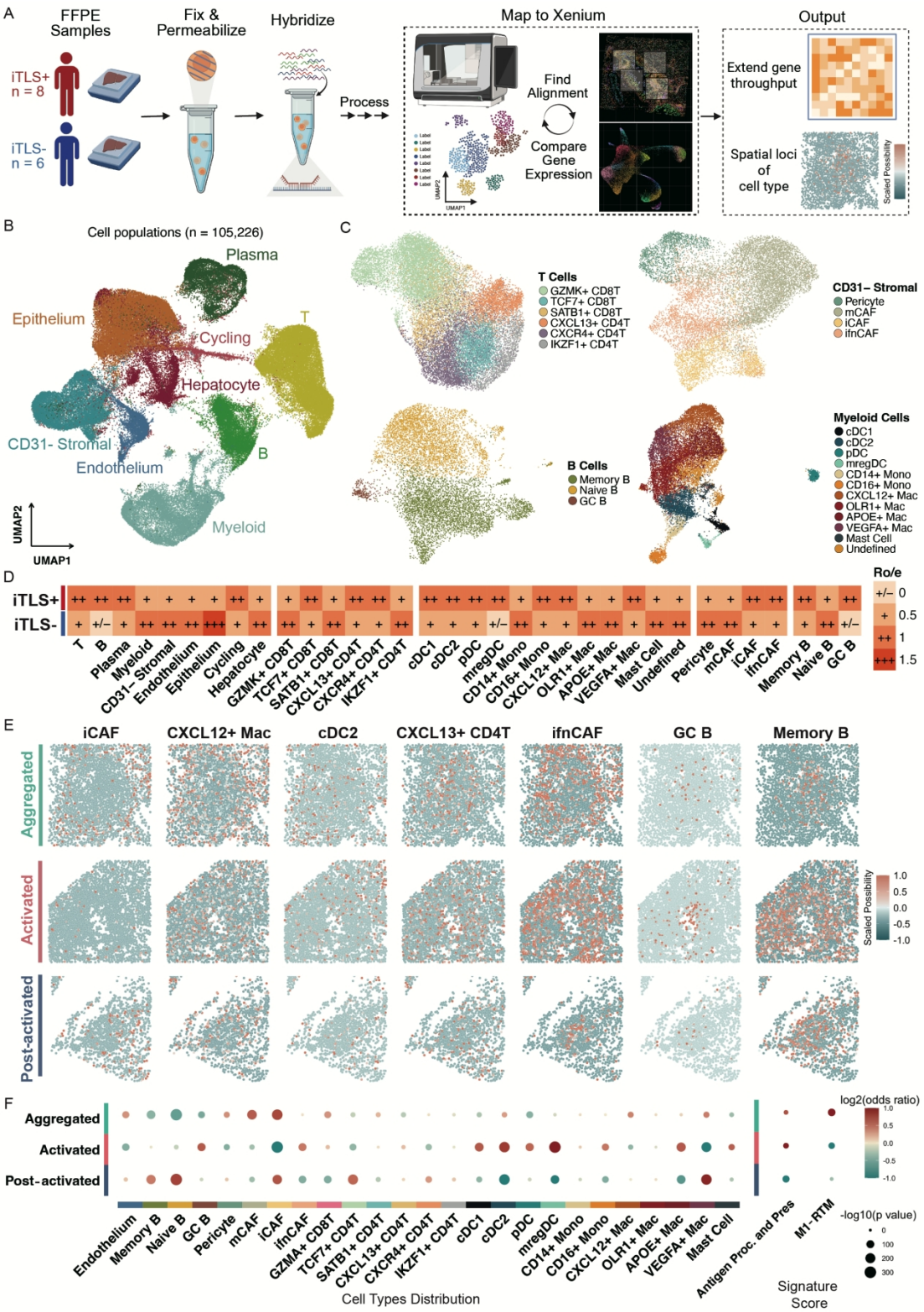

Figure 7. Single-nucleus RNA sequencing and cross-platform spatial mapping reveal TLS-associated immune programs and spatial configuratixons.

(A) Schematic of the integrative workflow combining 10x Chromium Flex single-nucleus RNA sequencing and Tangram-based spatial mapping to Xenium spatial transcriptomics coordinates.

1208 (B) UMAP projection of 105,226 nuclei across 14 iCCA samples (8 iTLS$^+$, 6 iTLS$^-$),
1209 showing major cell compartments including T cells, B cells, myeloid cells, stromal
1210 cells, endothelial cells, epithelial cells, cycling cells, and hepatocytes.
1211 (C) Refined clustering of T, B, myeloid, and stromal populations into functionally
1212 distinct subsets, including TCF7$^+$ CD8$^+$ T cells, CXCL13$^+$ CD4$^+$ T cells, germinal
1213 center B cells, iCAFs, IFNCAFs, and CXCL12$^+$ macrophages.
1214 (D) Ro/e analysis comparing cellular composition between iTLS$^+$ and iTLS$^-$ tumors at
1215 both major lineage and subset levels. iTLS$^+$ tumors are enriched for memory-type and
1216 antigen-presenting populations, while iTLS$^-$ tumors display elevated epithelial,
1217 stromal, and endothelial content.
1218 (E) Tangram-projected spatial mapping of Flex-identified subsets onto Xenium spatial
1219 transcriptomics coordinates reveals structured localization patterns. CXCL12$^+$
1220 macrophages and iCAFs localize to TLS periphery in Aggregated states, while
1221 CXCL13$^+$ CD4$^+$ T cells and memory B cells concentrate in TLS centers in Activated
1222 states.
1223 (F) Odds ratio (OR) analysis quantifying spatial distribution of mapped cell types
1224 across TLS molecular subtypes (Aggregated, Activated, Post-activated), validating
1225 subtype-specific enrichment patterns observed in spatial transcriptomic data.

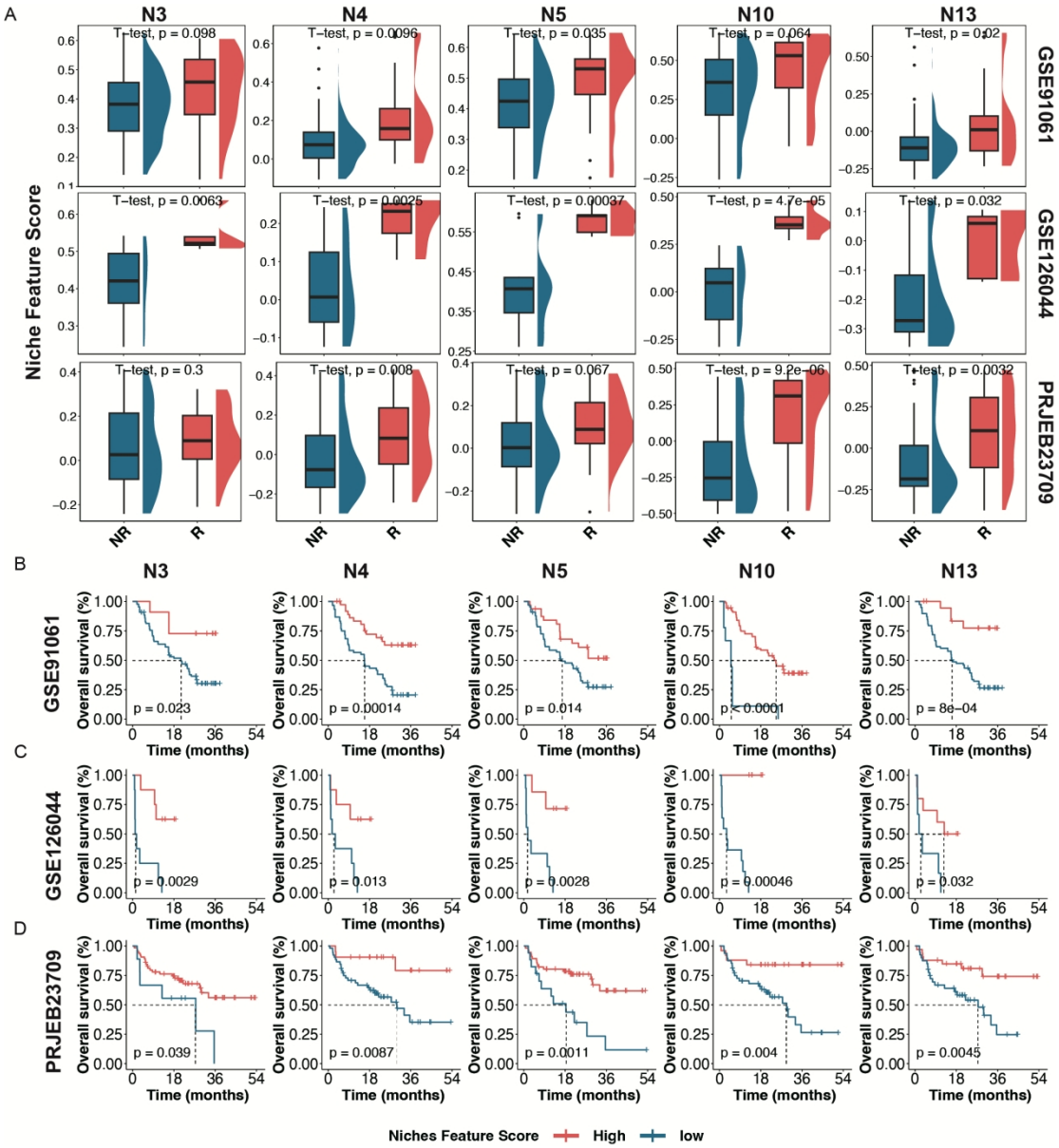

Figure 8. Clinical relevance of TLS-associated niches predicting immunotherapy benefit and survival outcomes.

(A) Boxplots showing the signature scores of five TLS-associated spatial niches: N3 (cDC2 & CXCL12^{+} Mac enriched), N4 (GC B & Naïve B enriched), N5 (iCAF & CCL9^{+} T & Mac enriched), N10 (ifnCAF, mregDC & GZMK^{+} CD8^{+} T enriched), and N13 (Memory B & CXCL13^{+} CD4^{+} T enriched) in responder versus non-responder groups across three independent immune checkpoint blockade cohorts (GSE91061, GSE126044, PRJEB23709). Signature scores were calculated using GSVA.

(B-D) Kaplan–Meier survival curves showing overall survival stratified by the signature score levels of TLS niche 3, 4, 5, 10, and 13 signatures in three independent immunotherapy-treated bulk RNA-seq datasets: (B) GSE91061 (anti–PD-1/anti-CTLA4–treated melanoma and non-small cell lung cancer), (C) GSE126044 (anti–PD-1–treated non–small cell lung cancer), and (D) PRJEB23709 (anti–PD-1/anti-CTLA4–treated melanoma and non-small cell lung cancer). Signatures were

computed using GSVA scores of niche-specific genes. p-values were calculated using the log-rank test.

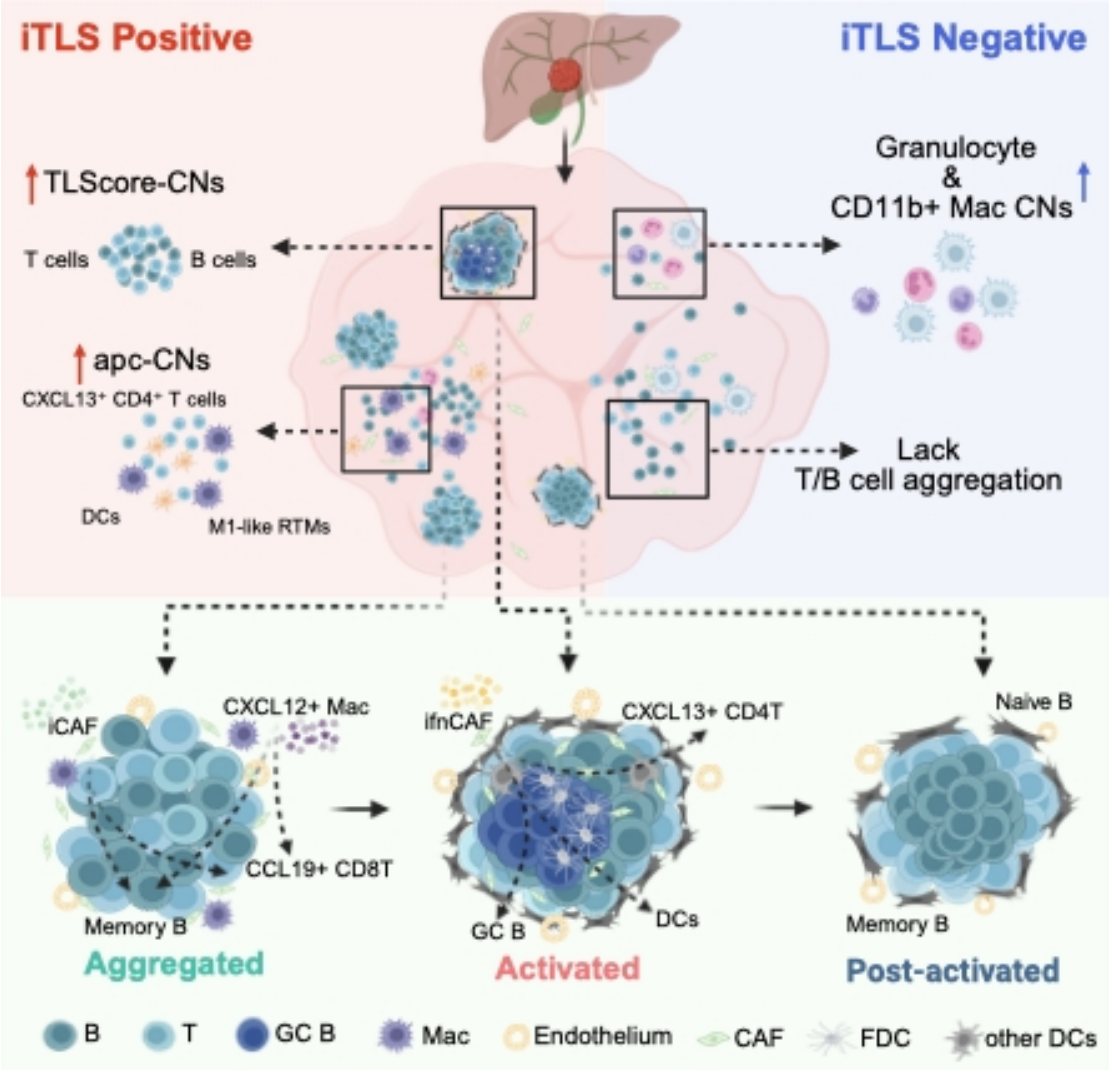

Figure 9. Graphical summary of iTLS-positive and iTLS-negative tumor microenvironments and the spatiotemporal trajectory of TLS maturation in iCCA.

(1) iTLS^{+} tumors harbor apc-CNs, which is consisted of M1-like RTM, dendritic cells, and CXCL13^{+} CD4^{+} T cells, as well as TLScore-CNs, which represent TLS existence. (2) iTLS- tumors, which means no TLS is not observed, enrich Granulocyte and CD11b+ Mac CNs. (3) TLSs are defined into a pseudo-temporal maturation continuum comprising aggregated, activated, and post-activated stages, each of which exhibits distinct microenvironmental changes.